A Point-Vortex Application to Vortex Stability, Evolution, and Statistical Equilibrium

John Persing and Michael T. Montgomery

Research Supported by the Office of Naval Research
Grant # ONR N00014-93-1-0456

Colorado State University

DEPARTMENT OF ATMOSPHERIC SCIENCE

PAPER NO. 587

A POINT-VORTEX APPLICATION TO VORTEX STABILITY, EVOLUTION, AND STATISTICAL EQUILIBRIUM

John Persing and Michael T. Montgomery

Research supported by the Office of Naval Research grant ONR-N00014-93-1-0456

Principal Investigator: Michael T. Montgomery

Department of Atmospheric Science

Colorado State University

Fort Collins, CO 80523

June 1995

Atmospheric Science Paper No. 587

ABSTRACT

The nonlinear evolution of an isolated, barotropic vortex in an infinite, frictionless domain is examined with a cloud of like-signed point-vortices. The stability of systems of point-vortices is reviewed as well as the stability of continuous systems possessing a sign reversal in the radial vorticity gradient like that observed in the inner core of hurricanes. The new result is the application of point-vortices to examine the evolution of a hurricane-like vortex system. Using a three-region approximation to the radial vorticity profile, the nondimensional problem can be reduced to two parameters. These are the inner radius of the vorticity maximum δ and the tangential wind speed at this radius $v_{\tan}(\delta)$. The relaxation time scale is on the order of five circuit times, and the relaxed vorticity profile ranges from near solid-body rotation to highly monopolar profiles. The relaxation time-scale and the monopolicity of the relaxed vorticity profile show some correlation to the strength of the linear instability in the initial system, although a more thorough examination of the parameter space is proposed to obtain a complete understanding of the processes involved in the relaxation.

ACKNOWLEDGEMENTS

This work was sponsored by the Office of Naval Research under grant ONR-N00014-93-1-0456 and by Martin-Marietta AMS/Industry Graduate Industry Fellowship for the 1993-1994 academic year. Numerical computations were performed using Hewlett Packard (HP) Apollo series computers belonging to the Montgomery Research Project. Programs were written in HP FORTRAN 9000 and in the Interactive Data Language (IDL) of Research Systems, Inc.

CONTENTS

Chapter 1

INTRODUCTION

A hurricane is typified by strong rotation, radial inflow and outflow, convection, cloudiness, etc. Evidently this is a complicated system, but it is of physical interest to study the fundamental properties of the rotation alone. It is proposed here that the basic rotational properties of a hurricane may be studied with point-vortex models and that results from such models may provide insight into the inviscid vortex climate for hurricane circulations. Both two-dimensional, non-divergent and quasi-geostrophic, shallow water formulations of the point-vortex model are integrated here to high accuracy. The initial states are designed to obtain insight into nonlinear relaxation processes in hurricanes. The two-dimensional, non-divergent simulations should also prove applicable to the circumpolar vortex, where the Rossby radius is large and friction is negligible.

The relaxation of an enhanced ring of vorticity near the outer edge of a vortex cloud is of particular meteorological interest and will be the subject of this thesis. Wind speed profiles for Hurricane Emily (1993) published by Burpee et al. (1994) (Figure 1.1) document changes in the vorticity distribution in the inner core of the storm. Within the radius of maximum winds, Figure (1.1a) depicts an approximately linear increase in wind speed, suggestive of a storm core that is in nearly solid body rotation with uniform vorticity. Figure (1.1e), on the other hand, depicts a more curved (concave-upward) profile in wind speed, indicative of a vorticity maximum near the eyewall. As a way of mimicking the latent heat released by moist convection in the eyewall, Möller and Smith (1994) model the evolution of a tropical cyclone forced by a heating maximum at a radius removed from the vortex axis. Figure (1.2) demonstrates a process by which tropospheric potential vorticity is accumulated at the radius of a heating maximum. The problem studied here has

been designed to replicate the eyewall vorticity maximum inferred from Figures (1.1e) and (1.2b). One numerical simulation of such a maximum (Guinn and Schubert (1993); Figure 1.3) implicates shear instabilities as an explanation for observations of polygonal eyewalls. This viewpoint is explored further in Edwards (1994). This thesis extends these studies by exploring both the nonlinear evolutionary dynamics and relaxed states of unstable vortices representative of the inner-core of a hurricane.

The basic properties of atmospheric vortices are often difficult to study due to the numerous physical influences that are present. The vortex may be fundamentally viewed as a rotating airmass overlaid with complicating elements. This simple picture is obscured by three-dimensional variability in temperature, pressure, friction, cloudiness, precipitation, radiation flux, and surface fluxes. The effect of such physical processes not only creates and destroys the vortex, but also plays an active role in defining its particular structure. The study of an "ideal" atmospheric vortex must be designed in light of these physical influences. One approach is to simulate the fully-complex vortex, peeling off one or another physical effect and observing the changes that result. In the alternative barotropic, inviscid approach, the basic vortex is studied by investigating a system without the effects of physical processes and three-dimensional structure.

Barotropic, frictionless flow has been the object of study for over a century, and as such serves as a strong basis for research. It is of interest to consider how some important aspect of a real-life system may be realized in this much simpler model and how the model then behaves. Both analytical and numerical tools are available in this effort. The Rayleigh stability criterion for rotating flows provides a sufficient criterion for shear stability for a given arrangement of vorticity in a vortex. Rayleigh's criterion, as well as Fjortoft's criterion and the semicircle theorem, is detailed in Gent and McWilliams (1986). Unstable arrangements can be further studied with more complex stability models. Whitaker and Turkington (1994) present a maximum entropy principle; when given a vorticity distribution, the technique computes the statistical properties of the equilibrium state consistent with the circulation, dispersion, and energy of the given system when the entropy is maximized. But, Rayleigh's sufficient criterion for stability can only serve as

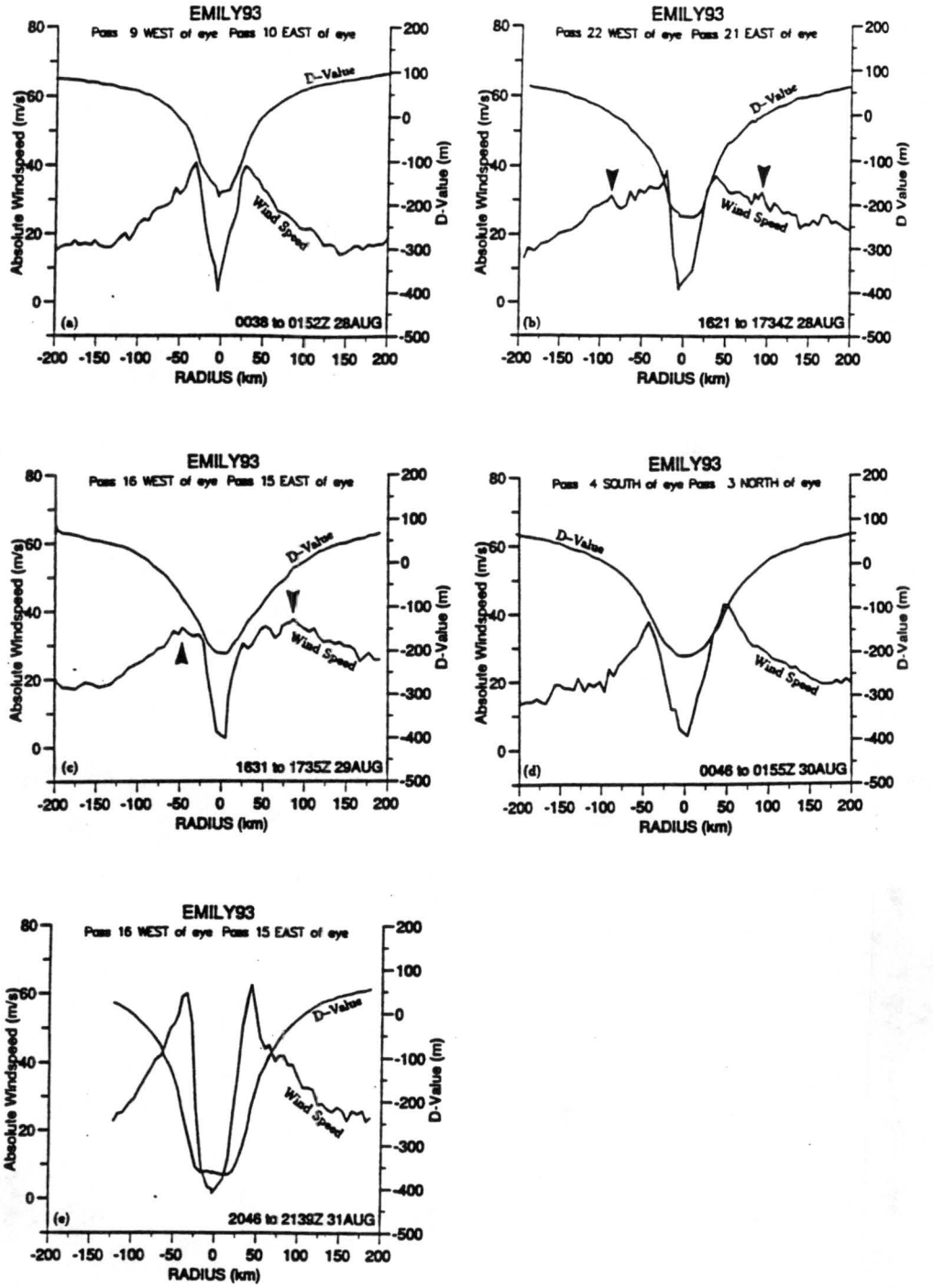

Figure 1.1: Flight-level (850 hpa) wind speed and D-values (departure of heights from environmental values) observed by Air Force Reserve reconnaissance aircraft flying in Hurricane Emily on five penetrations at different stages in the development of the storm (From Burpee et al. (1994)).

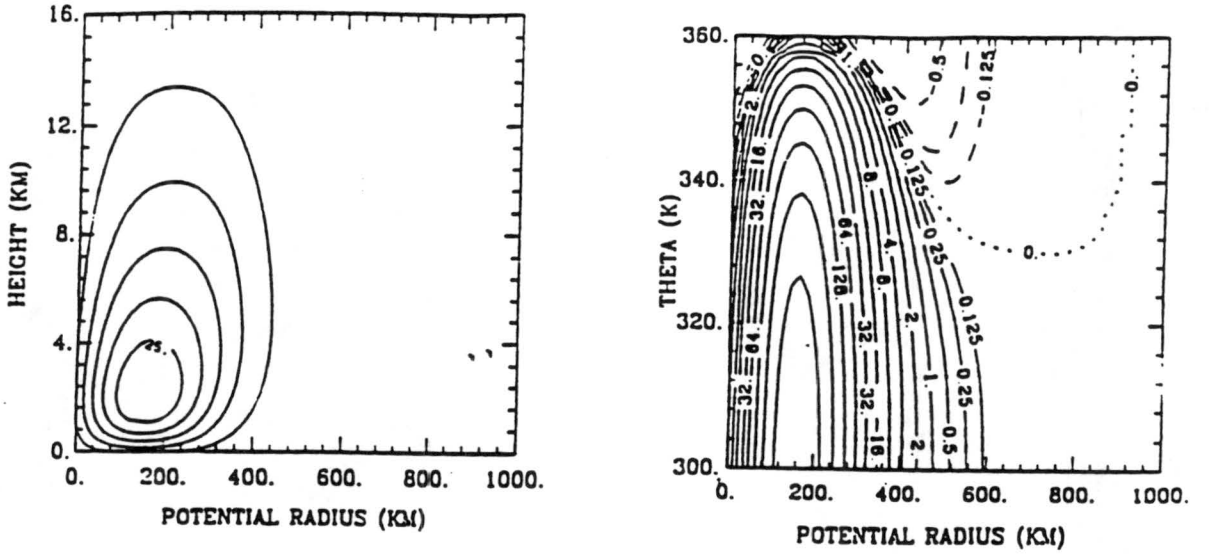

Figure 1.2: Results from numerical simulation of Möller and Smith (1994). (a) Isolines of the heating rate and (b) potential vorticity anomaly after 120 hours of simulation in an axisymmetric model. The potential radius of 150 km (near the heating rate and potential vorticity anomaly maxima) corresponds to an actual radius of approximately 37 km.

a necessary criterion for instability. Whitaker and Turkington construct the maximum entropy solution for two identical circular vortex patches in a large domain. In this model, merger always occurs, which contradicts known results (Melander et al., 1988). Thus, there is no guarantee that a given system will always relax to its maximum entropy state. Both analytical techniques fall short of a complete description of the dynamical evolution of the vortex system.

A more thorough understanding of barotropic vorticity dynamics requires numerical simulations of idealized equation sets with specific initializations. Balanced systems often capture important aspects of the development of a vortex. By making physical approximations to the mathematics, the family of different physical explanations may then be confined. The asymmetric balance theory (Shapiro and Montgomery, 1993) retains processes important for the development of hurricanes caused by low-wavenumber asymmetries while effectively filtering out the complicating influences of gravity waves. Further, full-blown numerical integrations can also capture important processes in the symmetrization and filamentation of a vortex. Processes involved in the relaxation of an unstable vortex can also be studied.

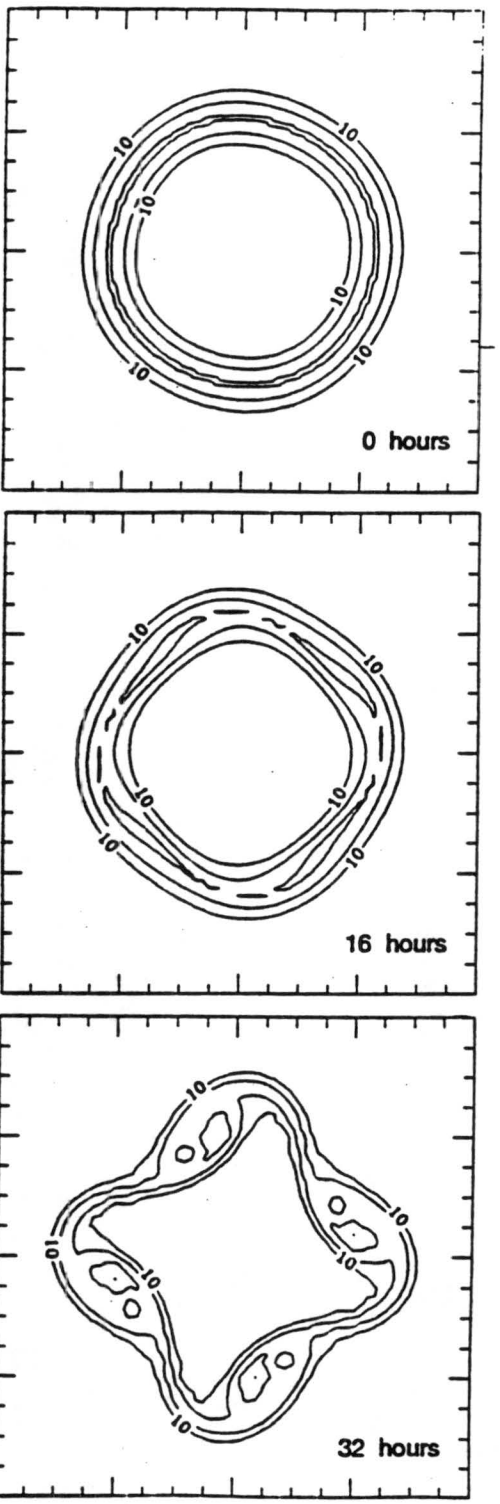

Figure 1.3: Potential vorticity contours at 0, 16, and 32 hours from the pseudo-spectral simulation of Guinn and Schubert (1993). Contours have units of $10^{-5}s^{-1}$ with an interval of $10^{-4}s^{-1}$.

There are several options for approximating the continuous fields in a form that is integrable by a computer. The two most common approaches are the grid-point and spectral representations. The grid-point model approximates the vortex with a finite array of equally spaced points at which field variables can be stored and computed. The spectral model represents the fields by a sum of a finite number of elementary basis functions. Both representations require a boundary, and so the vortex usually can only be studied in isolation by placing the boundaries of the domain a far distance away from the vortex. Then the physical properties of the boundaries have to be considered, often through the use of double-periodic boundary conditions or with rigid boundaries. Additionally, the truncation of the grid-point or spectral representation necessary to represent the system on a computer leads to inaccuracies in the flow at the smallest scale of motion, which are associated with the enstrophy cascade. To compensate, modelers are forced to add diffusion (friction) with the intent of selectively removing these small-scale disturbances. The contour dynamics technique (Zabusky et al., 1979) is an alternative representation of a vortex system. In this method, vorticity is represented as one or more finite areas of constant value. The perimeter of the finite areas is deformed by shear induced by the presense of the vorticity and its evolution represents the forecast. A computational challenge is presented as the perimeter evolves, obtaining extremely intricate structures. The perimeter is to a certain extent approximated by "contour snipping" and "contour suturing", which is necessary to represent the perimeter by a finite number of line segments. Within the limitations (representation, diffusion, boundaries, "contour surgery") of these numerical representations, valuable insights have been obtained regarding the development of vortices.

Barotropic models have proven useful in other areas of atmospheric science, in particular, the study of two-dimensional turbulence. In this field, grid-point models (Lilly, 1969) and spectral models (Fornberg, 1976; McWilliams, 1985) have been successfully applied. Of particular interest to this study is the point-vortex approach (Novikov, 1975; Carnevale, et al., 1991), which approximates vorticity with a finite number of singularities in vorticity that conserve the circulation of the original system. The vorticity field from

this model is inferred from the density and strength of the point-vortices. This system has no friction, and possesses certain invariants which can be maintained with sufficiently accurate numerical techniques. The point-vortex model has a strong footing in the literature of fluid dynamics and proves to have a simple mathematical form in an infinite domain.

The first logical step in trying to apply a point-vortex model to an atmospheric system is to replace the real world vortex with a single point-vortex. This was of interest to hurricane researchers in the 1950's and 1960's who sought numerical simplifications to speed forecasts on slow computers. Morikawa (1962) used a shallow water point-vortex to represent the storm. Kasahara (1957) and Kasahara and Platzman (1963) considered other time-invariant, axisymmetric representations. The approach in the three papers is to partition the wind into a vortex component and a steering component. The interactions between the vortex flow and the steering flow is handled differently between the three methods. The analytics used in their derivations provide interesting insights in vortex motion.

A further application of point-vortices would consider the interactions of a handful of vortices upon each other. Of note is the work of Stewart (1943), who modeled the stability of a system of anticyclones arranged in the subtropics as a polygon of vortices surrounding the north pole.

An extension of these ideas is to consider a cloud of many point-vortices. Onsager (1949) anticipated the now-established inverse energy cascade by applying statistical mechanical arguments to a system of point-vortices. Recently, Viecelli (1994) has extended these results to a system of like-signed vortices using fully non-linear computations. However, the cloud of vortices in these applications were not specifically intended to model a single, larger vortex, but simply served as a setting for the study of turbulence in a rotating system. An objective of this thesis is to extend these ideas by modeling the internal structure and development of a single vortex.

To demonstrate the ability of the point-vortex model to simulate the general properties of vortex evolution, consider two rather striking, canonical examples: axisymmetrization of an elliptical vortex patch and the merger of two identical vortices. Both problems

have been considered in testing the ability of the point-vortex model to repeat well-known results in the literature.

Axisymmetrization of an elliptical vortex has been considered by Melander et al. (1987) using a pseudo-spectral implementation of the quasi-geostrophic, shallow water system. The general character of the solution is for the lobes of the ellipse to first spiral away from the central vortex, then loop around as a ring, then surround the circular remnants of the vortex core. Figure (1.4) replicates the qualitative aspects of the continuous model using a modest number (160) of point-vortices. The spectral model initialization slopes off the vorticity from a constant value in a central elliptical area. The point-vortex approximation applies decreasing values of circulation to point-vortices in elliptical rings that are further from the center.

Using a vortex moment model, Melander et al. (1988) demonstrated that two identical circular patches of constant vorticity will merge if they are centered within 3.201 vortex radii of one another. Two different cases of output from the point-vortex model are shown in Figures (1.5) and (1.6), where the vortex patches are initially centered 3.18 and 4.24 vortex radii apart, respectively. These demonstrations conclusively show that clouds of point-vortices are useful tools for studying vortex development.

The problem of this thesis is to test the response of an unstable vortex in the form of a increase in the vorticity at the outer edge of a vortex cloud, first gleaning analytical results from a system with a small number of vortices, then examining the behavior of a system with a large number of vortices through numerical integration. The driving philosophy is to compare these results with other barotropic model results (particularly, spectral model output) to examine the process of relaxation in an unstable vortex in the absence of boundaries and diffusion, and to demonstrate the utility of the point-vortex model in modeling barotropic systems. The problem proves to be easily definable to a set of parameters which could be tested with a matrix of different initializations. With proper selection of the parameters, the vortex cloud will evolve nearly axisymmetrically. The simulations studied here focus on these nearly axisymmetric cases and take advantage of a powerful family of profiling analysis schemes.

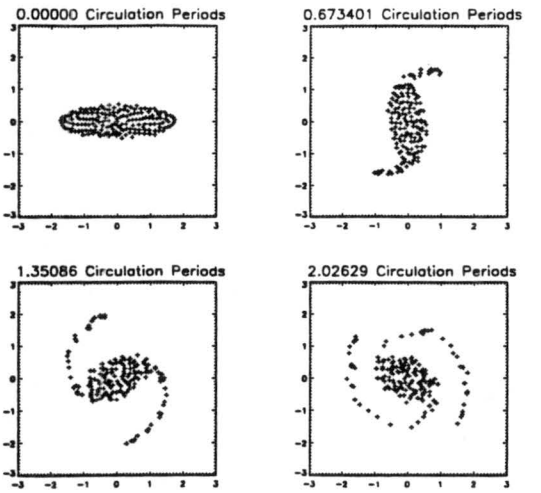

Figure 1.4: Evolution of a elliptical initialization of 160 point-vortices in a two-dimensional, non-divergent integration. The circuit period is determined from the angular velocity at the radius of the maximum tangential wind speed of the azimuthally averaged vortex after relaxation. The ejected spiral bands have a slower angular velocity than circular interior region.

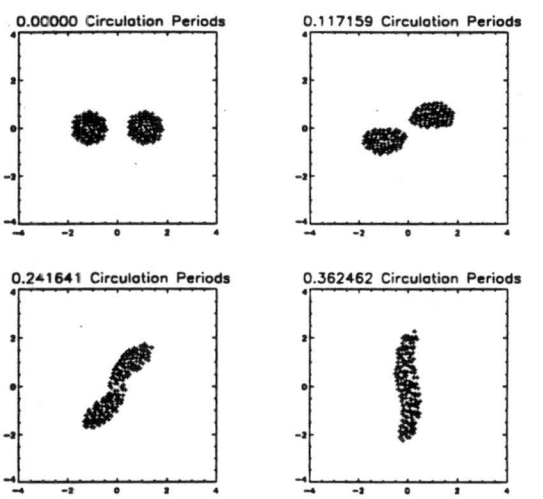

Figure 1.5: Evolution of two circular patches with 80 point-vortices each in a two-dimensional, non-divergent integration. The circuit period is determined from the angular velocity at the radius of maximum tangential wind speed of the azimuthal average about the centroid of the two vortex clouds near the beginning of the run.

Chapter 2 reproduces ring stability results for the point-vortex model and summarizes continuous field stability results of interest. Chapter 3 presents the descriptions of the mathematical models of this thesis, and Chapter 4 presents results of the numerical integrations, detailing several analysis schemes. Chapter 5 discusses the context of these results, indicating areas for future research.

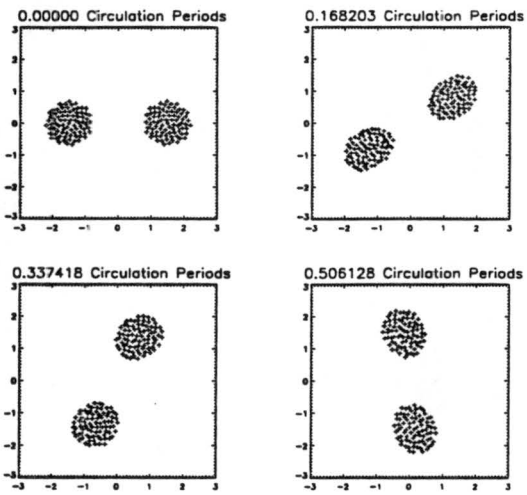

Figure 1.6: Evolution of two circular patches with 80 point-vortices each in a two-dimensional, non-divergent integration. The circuit period is determined from the angular velocity at the radius of maximum tangential wind speed of the azimuthal average about the centroid of the two vortex clouds near the beginning of the run.

Chapter 2

STABILITY

Observations suggest that oftentimes vorticity increases from the center of a hurricane to the eyewall (Figure 1.1e). This chapter summarizes several techniques for examining the stability of a vortex system with a maximum in vorticity located in a ring away from the center of the circulation. Three approaches are summarized which are canonical in analyzing the stability of a system of vortices arranged in a ring. Further stability analysis are summarized for continuous representations of the vorticity, and possible models for the physical mechanism of the instability are summarized.

2.1 Point-Vortex Ring Systems

2.1.1 Two-dimensional, non-divergent formulation

The proof of linear stability for seven or fewer vortices in a ring can be attributed, for the two-dimensional, non-divergent case, to Havelock (1941), who presented a simplification of an earlier analysis by Thompson (1882) who proved stability for a system of six vortices. The method of proof proceeds by linearizing the equations of motion for the non-divergent point-vortex model, with point-vortices intially located on a polygonal ring. For wave-like solutions, a dispersion relation is derived and a criterion for exponentially growing solutions may be deduced. Because of the historical significance of this proof, a summary of the derivation is given below.

In polar coordinates, the radial momentum equation takes the form

$$\frac{\mathrm{d}r_i}{\mathrm{d}t} = -\frac{1}{2\pi}\sum_{j\neq i}\frac{q_j r_j \sin(\theta_i - \theta_j)}{r_j^2 + r_i^2 - 2r_i r_j \cos(\theta_i - \theta_j)} \tag{2.1}$$

where r_i and θ_i are the positions of the i-th vortex and q_i is the circulation. Consider the case where all the vortices have the same circulation, q. The equilibrium state is such that all the vortices rotate about a common center at a constant rate given by

$$\omega = \frac{q\,(N-1)}{4\pi a^2} \tag{2.2}$$

where N is the number of vortices and a is radius of the ring. To linearize, consider the positions of the vortices to be defined

$$r_i = a + r_i' \tag{2.3}$$

$$\theta_i = \frac{2\pi i}{N} + \omega t + \theta_i'. \tag{2.4}$$

Substituting into the radial momentum equation (2.1), gives

$$\frac{\mathrm{d}a}{\mathrm{d}t} + \frac{\mathrm{d}r_i'}{\mathrm{d}t} = -\frac{q}{2\pi}\sum_{j\neq i} \frac{\left(a+r_j'\right)\sin\left(\frac{2\pi i}{N} + \theta_i' - \frac{2\pi j}{N} - \theta_j'\right)}{\left(a+r_j'\right)^2 + (a+r_i')^2 - 2\left(a+r_j'\right)(a+r_i')^2\cos\left(\frac{2\pi i}{N} + \theta_i' - \frac{2\pi j}{N} - \theta_j'\right)}. \tag{2.5}$$

After making the appropriate Taylor series approximations, and neglecting quadratic terms in the radial momentum equation (2.5) we obtain

$$\frac{\mathrm{d}r_i'}{\mathrm{d}t} = -\frac{q}{4\pi a}\sum_{j\neq i}\frac{\theta_{ji}'}{1-\cos w} \tag{2.6}$$

where $\theta_{ji}' = \theta_j' - \theta_i'$ and $w = 2\pi\,(j-i)\,/N$.

Similarly, starting from the tangential momentum equation,

$$r_i\frac{\mathrm{d}\theta_i}{\mathrm{d}t} = -\frac{1}{2\pi}\sum_{j\neq i}\frac{q_j\left\{-r_i + r_j\cos\left(\theta_i-\theta_j\right)\right\}}{r_j^2 + r_i^2 - 2r_ir_j\cos\left(\theta_i-\theta_j\right)}, \tag{2.7}$$

upon substituting the linearized definitions of the vortex positions (2.3, 2.4), (2.7) becomes

$$\left(a+r_i'\right)\frac{\mathrm{d}\left(\omega t+\theta_i'\right)}{\mathrm{d}t} = -\frac{q}{2\pi}\sum_{j\neq i}\frac{-\left(a+r_i'\right)+\left(a+r_j'\right)\cos\left(\frac{2\pi i}{N}+\theta_i'-\frac{2\pi j}{N}-\theta_j'\right)}{\left(a+r_j'\right)^2+(a+r_i')^2-2\left(a+r_j'\right)(a+r_i')\cos\left(\frac{2\pi i}{N}+\theta' i_- \frac{2\pi j}{N}-\theta_j'\right)}. \tag{2.8}$$

Carrying out similar Taylor series approximations gives

$$\left(a+r_i'\right)\omega + a\frac{\mathrm{d}\theta_i'}{\mathrm{d}t} = \frac{q}{4\pi a}\sum_{j\neq i}\left\{1+\frac{r_i'\cos w}{a\left(1-\cos w\right)} - \frac{r_j'}{a\left(1-\cos w\right)}\right\}. \tag{2.9}$$

To further simplify, (2.6) and (2.9) we take advantage of the relation

$$\sum_{j\neq i}\frac{1}{1-\cos w}=\frac{1}{6}\left(N^2-1\right). \tag{2.10}$$

The radial momentum equation (2.6) then becomes

$$\begin{aligned}
\frac{\mathrm{d}r_i'}{\mathrm{d}t} &= -\frac{q}{4\pi a}\sum_{j\neq i}\frac{\theta_{ji}'}{1-\cos w}\\
&= -\frac{q}{4\pi a}\sum_{j\neq i}\left(\frac{\theta_j'}{1-\cos w}-\frac{\theta_i'}{1-\cos w}\right)\\
&= -\frac{q}{4\pi a}\left(\sum_{j\neq i}\frac{\theta_j'}{1-\cos w}-\theta_i'\sum_{j\neq i}\frac{1}{1-\cos w}\right)\\
&= -\frac{q}{4\pi a}\left(\sum_{j\neq i}\frac{\theta_j'}{1-\cos w}-\frac{\theta_i'\left(N^2-1\right)}{6}\right)\\
&= \frac{q}{4\pi a}\left(\frac{\left(N^2-1\right)\theta_i'}{6}-\sum_{j\neq i}\frac{\theta_j'}{1-\cos w}\right).
\end{aligned} \tag{2.11}$$

The tangential momentum equation (2.9) also simplifies,

$$\begin{aligned}
\frac{\mathrm{d}\theta_i'}{\mathrm{d}t} &= -\frac{\omega r_i'}{a}+\frac{q}{4\pi a^3}\left\{r_i'\sum_{j\neq i}\frac{\cos w}{1-\cos w}-\sum_{j\neq i}\frac{r_j'}{1-\cos w}\right\}\\
&= -\frac{q\left(N-1\right)r_i'}{4\pi a^3}+\frac{q}{4\pi a^3}\left\{r_i'\sum_{j\neq i}\left[-1+\frac{1}{\cos w}\right]-\sum_{j\neq i}\frac{r_j'}{1-\cos w}\right\}\\
&= \frac{q}{4\pi a^3}\left\{r_i'\left[1-N+1-N+\sum_{j\neq i}\frac{1}{\cos w}\right]-\sum_{j\neq i}\frac{r_j'}{1-\cos w}\right\}\\
&= \frac{q}{4\pi a^3}\left\{r_i'\left[-2\left(N-1\right)+\frac{\left(N-1\right)\left(N+1\right)}{6}\right]-\sum_{j\neq i}\frac{r_j'}{1-\cos w}\right\}\\
&= \frac{q}{4\pi a^3}\left\{r_i'\left[\frac{1}{6}\left(N-1\right)\left(-12+N+1\right)\right]-\sum_{j\neq i}\frac{r_j'}{1-\cos w}\right\}\\
&= \frac{q}{4\pi a^3}\left\{\frac{1}{6}\left(N-1\right)\left(N-11\right)r_i'-\sum_{j\neq i}\frac{r_j'}{1-\cos w}\right\}.
\end{aligned} \tag{2.12}$$

Now, let us assume wavelike solutions for the vortex positions

$$r_i'=\alpha\exp\left(\frac{2ki\pi\mathrm{i}}{N}\right) \tag{2.13}$$

$$\theta_i'=\beta\exp\left(\frac{2ki\pi\mathrm{i}}{N}\right) \tag{2.14}$$

where $\mathrm{i} = \sqrt{-1}$ and the wavenumber $k \in \{0, 1, 2, \ldots, N-1\}$. Substituting these expressions into the radial equation (2.11) gives

$$\begin{aligned}
\frac{4\pi a}{q} \exp\left(\frac{2ki\pi\mathrm{i}}{N}\right) \frac{\mathrm{d}\alpha}{\mathrm{d}t} &= \frac{1}{6}\left(N^2-1\right)\beta \exp\left(\frac{2ki\pi\mathrm{i}}{N}\right) - \sum_{j\neq i} \frac{\beta \exp\left(\frac{2kj\pi\mathrm{i}}{N}\right)}{1-\cos w} \\
\frac{4\pi a}{q}\frac{\mathrm{d}\alpha}{\mathrm{d}t} &= \frac{1}{6}\left(N^2-1\right)\beta - \sum_{j\neq i} \frac{\beta \exp\left(\frac{2k(j-1)\pi\mathrm{i}}{N}\right)}{1-\cos w} \\
&= \frac{1}{6}\left(N^2-1\right)\beta - \sum_{j\neq i} \frac{\beta \exp\left(kw\mathrm{i}\right)}{1-\cos w} \\
&= \beta\left\{\frac{1}{6}\left(N^2-1\right) - \frac{1}{6}\left(N^2-1\right) + k\left(N-k\right)\right\} \\
&= k\left(N-k\right)\beta. \qquad (2.15)
\end{aligned}$$

The tangential equation (2.12) gives

$$\begin{aligned}
\frac{4\pi a^3}{q} \exp\left(\frac{2ki\pi\mathrm{i}}{N}\right) \frac{\mathrm{d}\beta}{\mathrm{d}t} &= \frac{1}{6}\left(N-1\right)\left(N-11\right)\alpha \exp\left(\frac{2ki\pi\mathrm{i}}{N}\right) - \sum_{j\neq i} \frac{\alpha \exp\left(\frac{2kj\pi\mathrm{i}}{N}\right)}{1-\cos w} \\
\frac{4\pi a^3}{q}\frac{\mathrm{d}\beta}{\mathrm{d}t} &= \frac{1}{6}\left(N-1\right)\left(N-11\right)\alpha - \sum_{j\neq i} \frac{\alpha \exp\left\{\frac{2k(j-i)\pi\mathrm{i}}{N}\right\}}{1-\cos w} \\
&= \frac{1}{6}\left(N-1\right)\left(N-11\right)\alpha - \sum_{j\neq i} \frac{\alpha \exp\left(kw\mathrm{i}\right)}{1-\cos w} \\
&= \alpha\left\{\frac{1}{6}\left(N-1\right)\left(N-11\right) - \frac{1}{6}\left(N-1\right)\left(N+1\right) + k\left(N-k\right)\right\} \\
&= \alpha\left\{\frac{1}{6}\left(-12\right)\left(N-1\right) + k\left(N-k\right)\right\} \\
&= \alpha\left\{k\left(N-k\right) - 2\left(N-1\right)\right\}. \qquad (2.16)
\end{aligned}$$

Equations (2.15, 2.16) constituted two coupled differential equations for the unknowns (α and β). Assuming exponential solutions of the form $\alpha = \hat{\alpha}\exp(\lambda t)$ and $\beta = \hat{\beta}\exp(\lambda t)$ in (2.15) and solving for λ gives

$$\lambda = \frac{\hat{\beta}}{\hat{\alpha}} \frac{k\left(N-k\right)}{4\pi a/q}. \qquad (2.17)$$

Substituting (2.17) into (2.16) then gives

$$\lambda = \frac{\hat{\alpha}}{\hat{\beta}} \frac{k\left(N-k\right) - 2\left(N-1\right)}{4\pi a^3/q}. \qquad (2.18)$$

N | k	0	1	2	3	4	5	6	7	8	9
2	S	S								
3	S	S	S							
4	S	S	S	S						
5	S	S	S	S	S					
6	S	S	S	S	S	S				
7	S	S	S	N	N	S	S			
8	S	S	S	U	U	U	S	S		
9	S	S	S	U	U	U	U	S	S	
10	S	S	S	U	U	U	U	U	S	S

Table 2.1: Linear Stability of a Non-Divergent Ring

Multiplying Equations (2.17) and (2.18) together gives the desired dispersion relation

$$\begin{aligned} \lambda^2 &= \frac{k(N-k)\{k(N-k)-2(N-1)\}}{4^2\pi^2a^4/q^2} \\ &= \left(\frac{q}{4\pi a^2}\right)^2 k(N-k)\{k(N-k)-2(N-1)\}. \end{aligned} \tag{2.19}$$

Since k is constrained such that $0 \leq k < N$, the quantity $(N-k) > 0$. In addition, $\left(\frac{q}{4\pi a^2}\right)^2$ is also positive. Thus, λ^2 may only be negative when

$$2(N-1) > k(N-k) \tag{2.20}$$

$$N > \frac{2-k^2}{2-k}. \tag{2.21}$$

When λ^2 is negative (λ is imaginary), the solutions are sinusoidal in time, and thus the system is exponentially stable. When λ is real, there are two solutions ($\lambda > 0$ and $\lambda < 0$), one of which is an exponentially growing solution, thus the system is linearly unstable. The stability of the system is then sensitive to the number of vortices N. For a wavenumber one perturbation ($k = 1$), $N > 1$, so this perturbation is always stable. Similarly, the wavenumber two perturbation is stable. For wavenumbers higher than two, the stability relation provides stable solutions when $N < \frac{2-k^2}{2-k}$. Table (2.1) shows an evaluation of the stability. Here the wavenumber of the instability is plotted against the number of vortices in the ring; S indicates linear stability, N indicates neutral linear stability, and U indicates linear instability. The result of this is that a system of less than seven vortices is stable, for seven vortices it is neutrally stable, and for more than seven vortices, the system is

linearly unstable. If we consider the problem of very many vortices arranged on a ring to be a very crude representation of a eyewall maximum in vorticity, then we see the earliest hint for the possibility then that this situation may be unstable.

The stability of the ring system can be affected with the addition of a fixed central vortex. Havelock demonstrates how the proof may be extended. Equation (2.8) is modified by the addition of a term to the right hand side

$$(a+r_i')\frac{\mathrm{d}\left(\omega t+\theta_i'\right)}{\mathrm{d}t}= \\ -\frac{q}{2\pi}\sum_{j\neq i}\frac{-(a+r_i')+\left(a+r_j'\right)\cos\left(\frac{2\pi i}{N}+\theta_i'-\frac{2\pi j}{N}-\theta_j'\right)}{\left(a+r_j'\right)^2+(a+r_i')^2-2\left(a+r_j'\right)(a+r_i')\cos\left(\frac{2\pi i}{N}+\theta' i_-\frac{2\pi j}{N}-\theta_j'\right)} \\ +\frac{q_0}{2\pi a^2}(a-r_i') \tag{2.22}$$

where q_0 is the strength of the central vortex. The proof follows along the same lines as above, and the resulting dispersion relation (2.19) becomes

$$\lambda^2=k(N-k)\left\{k(N-k)-2(N-1)-\frac{4q_0}{q}\right\}. \tag{2.23}$$

The stability of the system is promoted if the central vortex is of the same sign as the ring vortices, because λ^2 is made more negative.

2.1.2 Quasi-geostrophic, Shallow-water formulation

The stability of a ring of vortices in a shallow water system is shown by Stewart (1945) for up to six vortices, and for seven vortices if the Rossby radius of deformation is sufficiently large. His study was concerned with the possible stability of a system of semi-permanent high pressure systems as is commonly found in the subtropics. He also inferred the stability result for the addition of a central vortex. A counter-rotating vortex (as one might model the semi-permanent polar vortex in his example) promotes the instability of the ring.

Stewart (1945) considers the shallow water system for a rotating disk and finds that the velocity resulting from a single point-vortex (defined by a singularity in potential vorticity) must be solved for with a complicated second order differential equation

$$\frac{\mathrm{d}^2v_{\tan}}{\mathrm{d}\rho^2}+\frac{1}{\rho}\frac{\mathrm{d}v_{\tan}}{\mathrm{d}\rho}-\left(1+\frac{1}{\rho^2}\right)v_{\tan}=\frac{1}{\rho}v_{\tan}^2 \tag{2.24}$$

where ρ is a dimensionless parameter related to distance. After linearization the system simplifies and the solution for the free-surface height is simply a Bessel function. The linearization removes most of the effects of the rotation of the domain, which then serves only as a coefficient on the x- and y-coordinates. The streamfunction is $AK_0(\rho)$, where K_0 is the zeroth order modified Bessel function of the second kind, ρ is a distance non-dimensionalized by the Rossby deformation radius, and A is an arbitrary constant. Stewart numerically demonstrates the similarity between the Bessel function linear solution and the solution for the non-linear formulation. The nonlinear solutions are similar for cyclones and anticyclones of the same strength, but the anticyclone solution is weaker.

Stewart tests the stability of the ring arrangement of vortices for his linearized system. His analysis shows that the system is stable for six or fewer vortices. The stability can be extended to seven vortices if the non-dimensional length scale of the ring is sufficiently large, this is the case as the shallow-water system is represented by a very small fluid depth, and the system approaches the two-dimensional result.

Morikawa and Swenson (1971) extended the result of Stewart (1945) by systematically testing the stability of vortex systems with variations in the number of vortices, N, in the ring, the inverse Rossby radius, κ, and the strength, q_0, of the central vortex. Neutral stability curves for their analysis of the stability of the ring vortices are shown in Figure (2.1a). We can see, for example, that if there is no central vortex ($q_0 = 0$) and the inverse Rossby radius vanishes ($\kappa = 0$), Figure (2.1a) indicates that a ring of seven vortices is neutrally stable, which reproduces Havelock's analysis. We can also note that the addition of the central vortex promotes the stability of systems with more ring vortices, verifying the analysis of Stewart and Havelock. Increases in κ (decreases in the Rossby radius) lead to a more unstable ring system. This occurs because a given vortex in a ring system with large κ is proportionately more greatly influenced by neighboring vortices than in a system with small κ. A vortex and its nearest neighbors then could be crudely modeled as a system of three equal vortices that has an equilibrium solution only when arranged as an equilateral triangle; this is distinctly not the case, so we can logically conclude that the ring system is not stable.

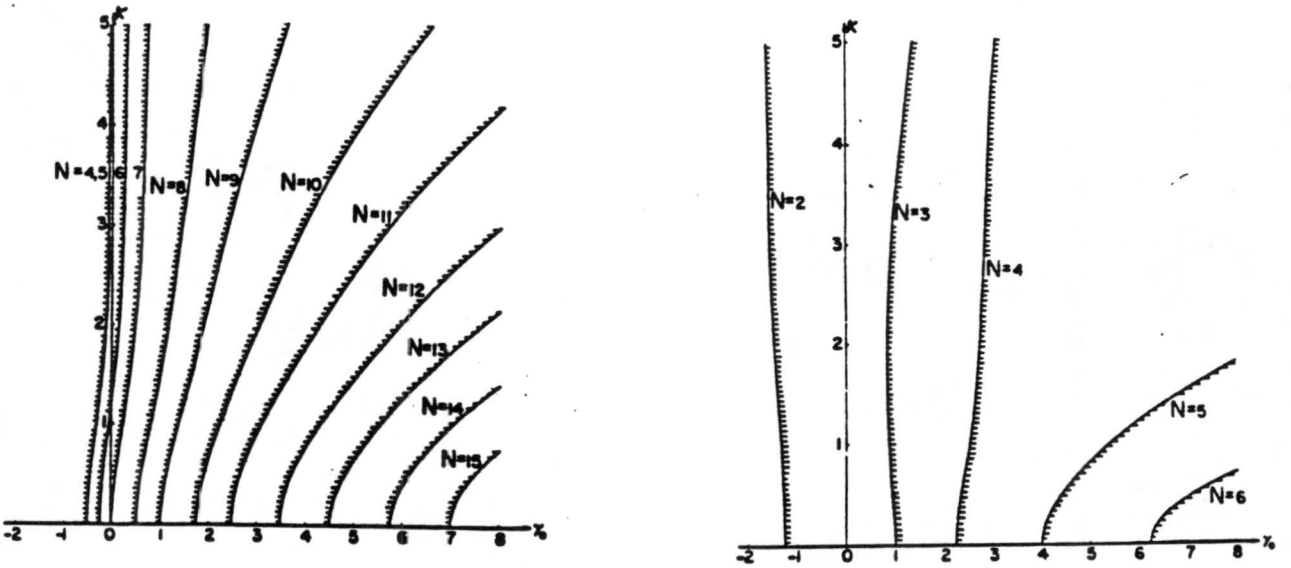

Figure 2.1: (a) Neutral stability curves for ring vortices where stable regions lie to the right of each curve. (b) Neutral stability curves for the center vortex where stable regions lie to the left of each curve. (Both figures from Morikawa and Swenson, 1971).

Figure (2.1b) is similar to Figure (2.1a), but shows neutral stability curves for the center vortex. In a system where $\kappa = 0$, a zero-strength central vortex is stable if there are three or more vortices in the ring. As the central vortex obtains more positive strength, more vortices are required in the ring for continued stability. The stability of the entire system is assured when both the ring stability and central vortex stability is considered in intersection.

2.2 Continuous Ring Systems

Edwards (1994) and Gent and McWilliams (1986) contain excellent summaries of different techniques for diagnosing the stability/instability of an axisymmetric distribution of vorticity. Some of these schemes are of particular interest for this thesis and are summarized below. Rayleigh's sufficient criterion for stability in rotating flows is valuable for insight. Since it states that a vortex profile without a reversal of sign in the gradient of vorticity will be stable, visual inspection of the vorticity profile is frequently all that is required to determine stability. When Rayleigh's sufficient criterion does not apply, more sophisticated schemes are required.

Michalke and Timme (1967) consider the stability of a cylindrical vortex sheet in a three-dimensional, non-divergent setting. This system could be approximately modeled in a two-dimensional setting by a point-vortex ring system with a large number of vortices, so we anticipate that this system will be unstable. The velocity profile is described by

$$\begin{aligned} v_{\tan} &= 0 \qquad \text{for} \qquad 0 \le r < R \\ v_{\tan} &= \frac{V_0 R}{r} \qquad \text{for} \qquad r > R \end{aligned} \tag{2.25}$$

where $v_{\tan}(R) = V_0$ at the radius of the vortex sheet. This is depicted in Figure (2.2a).

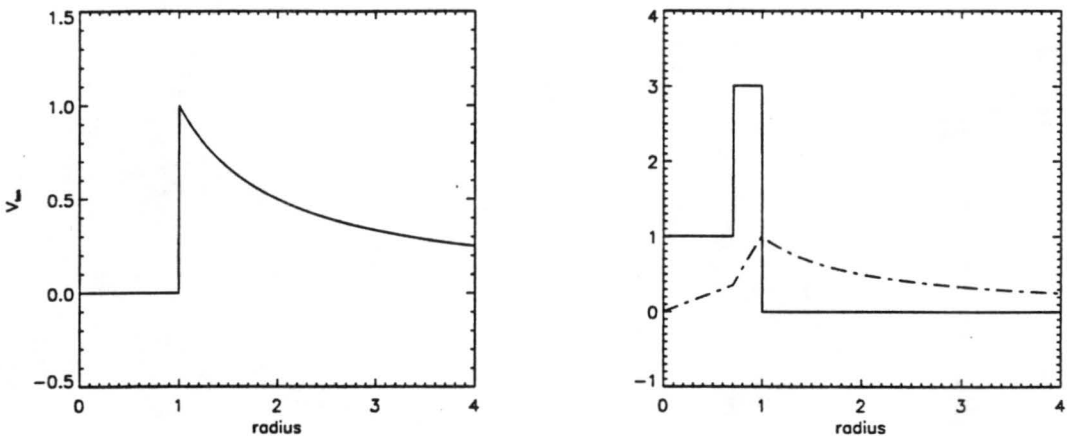

Figure 2.2: (a) Velocity profile for the cylindrical vortex sheet. (b) Vorticity (solid curve) and velocity (dashed curve) profiles for the three-region model.

Michalke and Timme consider disturbances of the form $\exp[\mathrm{i}(m\theta + kz - \beta t)]$ where the positive integer m is the wavenumber of the disturbance along the angular coordinate θ, k is the vertical wavenumber, and the real part of β is the cyclic frequency and the imaginary part is the temporal growth rate. Purely horizontal disturbances an diagnosed from the resulting analysis by setting $k = 0$; the resulting system proves to be unstable for $m \ge 1$.

Michalke and Timme extend the analysis to a situation where the vorticity is distributed in three regions

$$\begin{aligned} \zeta(r) &= \zeta_1 \qquad \text{in} \qquad 0 \le r < \delta \\ \zeta(r) &= \zeta_2 \qquad \text{in} \qquad \delta < r < 1 \\ \zeta(r) &= 0 \qquad \text{in} \qquad 1 < r < \infty \end{aligned} \tag{2.26}$$

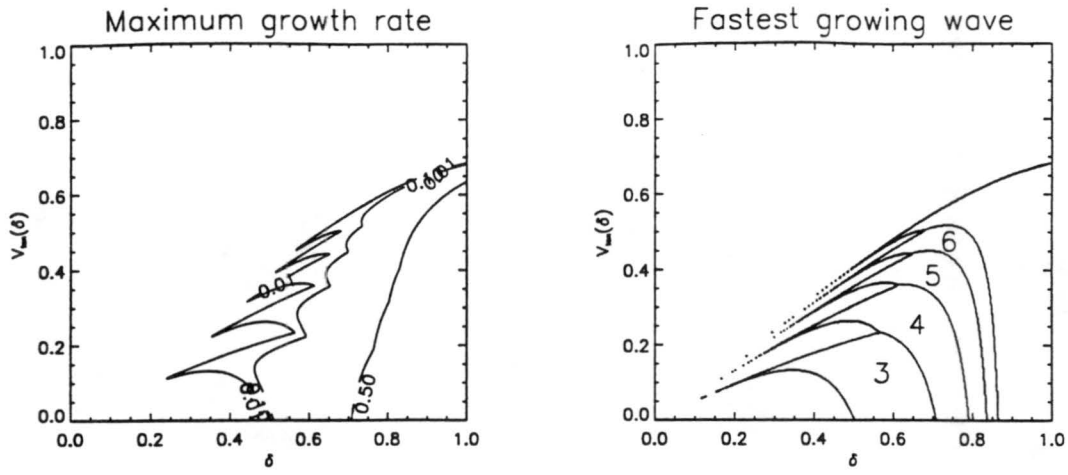

Figure 2.3: (a) Contours of the exponential growth rate of the fastest growing unstable mode. (b) The fastest growing mode, where the integers denote azimuthal wavenumbers.

as depicted, for example, by the solid curves in Figure (2.2b). Vertical disturbances are neglected at the start of the analysis ($k = 0$); thus it proves applicable to the cases studied in this thesis. Figure (2.3) summarizes the growth rates for the fastest growing modes, while Figure (2.4) depicts the growth rates for azimuthal waves 3, 4, 5, and 6. The non-dimensional velocity-scale is defined by $v_{\tan}(1) = 1$, which, together with the spatial-scale, define the non-dimensional time-scale of the figures. We note from these graphs that instabilities are more likely and grow faster as $\delta \rightarrow 1$. The case of a cylindrical vortex sheet analyzed above would be modeled here when $\delta = 1$ and $v_{\tan}(\delta) = 0$. We also note that δ and $v_{\tan}(\delta)$ can be selected so that the system may be stable. The Rankine vortex, which is known to be stable, can be modeled by setting $\delta = 0$. Also, where $v_{\tan}(\delta) > \delta$, we can also expect stable solutions because Rayleigh's sufficient criterion is satisfied.

Edwards (1994) extends this result for an arbitrary number of constant vorticity regions. Edwards tested the stability of a 64-region approximation of a Gaussian distribution of vorticity centered at a large radius so that the vorticity is near zero at the origin. For comparison, the system could be crudely modeled with Michalke and Timme's analysis by setting $v_{\tan}(\delta) = 0$. As $\delta \rightarrow 1$, the system could be compared to the 64-region model with decreases in the Gaussian half-width. As the Gaussian half-width decreases, higher wavenumber asymmetries are more evident in the 64-region model. This result captures

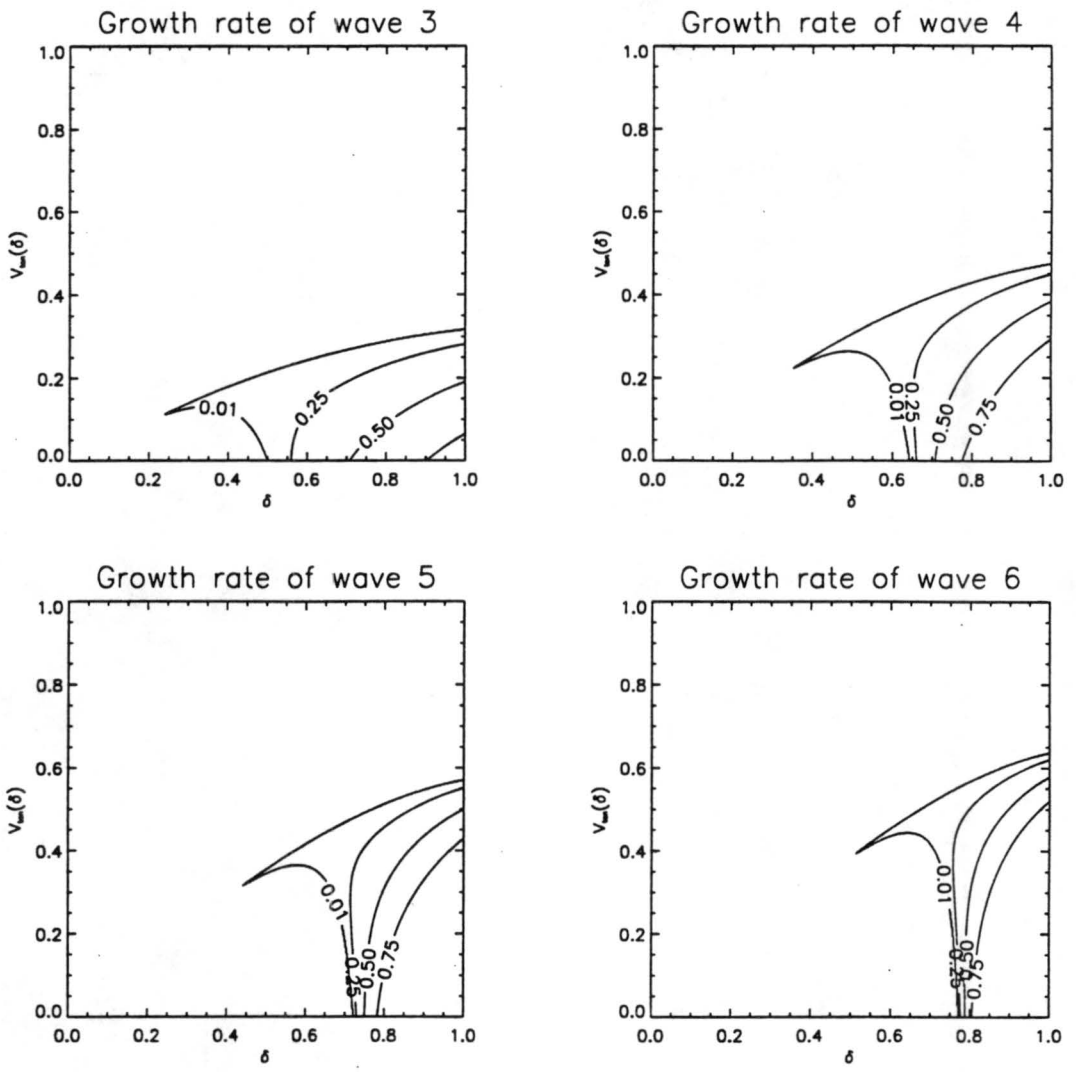

Figure 2.4: Contours of the exponential growth rates for four modes ($m = 3, 4, 5, 6$) for the 3-region model. The growth rates are non-dimensionalized time, which is defined by the characteristic shear, based on the maximum tangential velocity and the radius of maximum winds.

much of the character of the result of Figure (2.3b). Edward's result, though, shows that the Gaussian vorticity distribution is also unstable for wavenumber 2 perturbations; wavenumber 2 is stable in the three-region model.

Chapter 3

THE MODELS

This chapter develops two different versions of the point-vortex model. The quasi-geostrophic shallow water model is the most general form. The two-dimensional, non-divergent case can be obtained from the shallow water model by allowing the inverse Rossby radius to vanish. The differing development (and integration) for the non-divergent model is motivated by both historical and practical reasons. The non-divergent model is the older of the two models, and carries with it a large body of literature. Its simplicity lends itself to both simple analytical understanding as well as faster numerical computation. The relative insensitivity between the two numerical integrations for small values of the inverse Rossby radius is demonstrated in Chapter 4.

3.1 Two-Dimensional Non-Divergent Point Vortex Model

3.1.1 Analytical Description

The inviscid, two-dimensional non-divergent point-vortex model is the simplest of the models studied in this thesis. Batchelor (1967) develops this model (referred to hereafter as the 2d model) in his fluid dynamics text, and his description is summarized here. In two-dimensional domain flow, vorticity consists only of the vertical component defined by

$$\zeta = \frac{\partial v}{\partial x} - \frac{\partial u}{\partial y} \tag{3.1}$$

where u and v are x- and y-components of the velocity, respectively. For the idealized flows considered, the domain is unbounded and thus for flow to vanish at infinity, the irrotational component of the wind must be discarded. In this case, the wind may be derived solely from the streamfunction:

$$\psi(x,y) = \frac{1}{4\pi} \int \zeta(x',y') \ln\left\{(x-x')^2 + (y-y')^2\right\} \, \mathrm{d}A(x',y') \tag{3.2}$$

where integration occurs over the entire infinite domain. The wind flow consistent with (3.2) is

$$u(x,y) = -\frac{1}{2\pi}\int \frac{y-y'}{(x-x')^2+(y-y')^2}\,\zeta(x',y')\;\mathrm{d}A(x',y') \tag{3.3}$$

$$v(x,y) = \frac{1}{2\pi}\int \frac{x-x'}{(x-x')^2+(y-y')^2}\,\zeta(x',y')\;\mathrm{d}A(x',y')\,. \tag{3.4}$$

The vorticity is described by

$$\zeta = \nabla^2\psi. \tag{3.5}$$

The point-vortex approach allows the continuous-field vorticity distribution to be replaced by a finite number of point-vortices constructed so that the total circulation of the system is still preserved. To account for the development of the entire system, it is only necessary now to account for the development through time of the limited number of point-vortices. The streamfunction consistent with a single point-vortex is

$$\psi(x,y) = \frac{1}{4\pi}q\,\ln\left\{(x-x_1)^2+(y-y_1)^2\right\} \tag{3.6}$$

where q is the integrated circulation of the point-vortex located at (x_1, y_1). Since the invertibility problem is linear, for N point-vortices we have:

$$\psi(x,y) = \frac{1}{4\pi}\sum_i q_i\,\ln\left(r_i^2\right) \tag{3.7}$$

where i is indexed on the vortices, and r_i is the distance from the point of evaluation (x, y) to the position of the ith vortex (x_i, y_i).

Since a vortex will not advect itself, its motion is due to the velocities induced from all other vortices. The motion of vortex i is then described by

$$\frac{\mathrm{d}x_i}{\mathrm{d}t} = -\frac{1}{2\pi}\sum_{j\neq i}\frac{q_j\,(y_i-y_j)}{r_{ij}^2} \tag{3.8}$$

$$\frac{\mathrm{d}y_i}{\mathrm{d}t} = \frac{1}{2\pi}\sum_{j\neq i}\frac{q_j\,(x_i-x_j)}{r_{ij}^2} \tag{3.9}$$

where r_{ij} is the distance between vortices i and j. Aref (1983) applies principles regarding the Hamiltonian properties of the point-vortex system to state that the model is integrable for up to three vortices. To obtain solutions of (3.8, 3.9) for a large number of vortices a numerical integration scheme is generally neccessary. In this thesis we use a fixed-timestep, fourth-order Runge-Kutta algorithm programmed in FORTRAN. Appendix A details the accuracy of the integration.

3.1.2 Non-dimensionalization

For the purposes of numerical integration, it proves convenient to non-dimensionalize (3.8, 3.9). Consider the continuous representation of the x-component of the velocity

$$\frac{\mathrm{d}x}{\mathrm{d}t} = -\frac{1}{2\pi}\int \frac{y-y'}{r'^2}\zeta' \,\mathrm{d}A' \tag{3.10}$$

where primed quantities are considered at the source point and r' is the distance from the observation point to source point. Since only the advective dynamics within the vortex core are of interest, define the characteristic length, R, to be the radius of maximum winds. Then define the following quantities

$$x \equiv x_* R \tag{3.11}$$

$$y \equiv y_* R \tag{3.12}$$

$$y' \equiv y'_* R \tag{3.13}$$

$$r' \equiv r'_* R \tag{3.14}$$

where the starred quantities are non-dimensional. Also, define

$$t \equiv t_* T \tag{3.15}$$

where T is a characteristic time scale to be determined below.

Substituting into (3.10)

$$\frac{\mathrm{d}\,(x_* R)}{\mathrm{d}\,(t_* T)} = -\frac{1}{2\pi}\int \frac{y_* R - y'_* R}{r'^2_* R^2}\,\zeta' \,\mathrm{d}\,(x_* R)\;\mathrm{d}\,(y_* R) \tag{3.16}$$

and simplifying gives

$$\frac{\mathrm{d}x_*}{\mathrm{d}t_*} = -\frac{T}{2\pi}\int \frac{(y_* - y'_*)}{r'^2_*}\,\zeta' \,\mathrm{d}x_*\,\mathrm{d}y_*. \tag{3.17}$$

Non-dimensionalize the vorticity

$$\zeta' = \frac{\zeta'_*}{T} \tag{3.18}$$

and define T such that $\zeta'_* = 1$ on average in the interior of the storm (i.e. inside the radius R). This implies that the total circulation of the non-dimensional system is π. Equation

(3.10) can now be represented in non-dimensional form, from which model equations will be derived

$$\frac{\mathrm{d}x_*}{\mathrm{d}t_*} = -\frac{1}{2\pi}\int \frac{(y_* - y'_*)}{r'^2_*}\,\zeta'\,dx_*\,dy_*. \tag{3.19}$$

Since this equation is formally identical to (3.10), discretization follows in the same way as Section (3.1.1). The forecast equation is thus

$$\frac{\mathrm{d}x_{i_*}}{\mathrm{d}t_*} = -\frac{1}{2\pi}\sum_{j\neq i}\frac{q_{j_*}\,(y_{i_*} - y_{j_*})}{r^2_{ij_*}}. \tag{3.20}$$

To fix ideas, consider values from a typical storm (from Hurricane Emily based on observations of Burpee et al. (1994)). Consider the maximum wind, $v_{\max}$, to be 62 m s^{-1} and assume it occurs at 43 km radius. If we assume circularly symmetric flow, then the mean angular velocity is

$$Q = \frac{v_{\max}}{R} \sim \frac{62\ \mathrm{m/s}}{43000\ \mathrm{m}} \doteq 1.45 \times 10^{-3}\mathrm{s}^{-1} \tag{3.21}$$

and the mean vorticity is

$$\zeta' = 2Q \doteq 2.9 \times 10^{-3}\mathrm{s}^{-1}. \tag{3.22}$$

We defined T in Equation (3.18) such that

$$T = \frac{\zeta'_*}{\zeta'} \doteq \frac{1}{2.9 \times 10{-}3/\mathrm{s}} \doteq 345\ \mathrm{s} = 5\frac{3}{4}\ \text{minutes}. \tag{3.23}$$

Thus the observed circuit time is

$$\frac{2\pi R}{v_{\max}} \doteq 4360\ \mathrm{s} \doteq 72.6\ \text{minutes} = 4\pi T. \tag{3.24}$$

The non-dimensionalized circulation time in the 2d model is then 4π.

3.1.3 Integral Invariants

As described by Batchelor (1967), the 2d model carries with it integral invariants. Each invariant is derived from a physical conservation principle, such as linear momentum, angular momentum, and energy. Due to the unbounded domain, constant infinity terms arise in the derivation. Since the infinity terms are constant, the remaining, finite terms in the invariant must also be constant. These remaining terms are referred to here as the

invariants. The momentum invariants are divided by the total circulation in order to give geometrical insight. The two invariants derived from linear momentum conservation are related to the centroid of the system in x- and y-coordinates:

$$X = \frac{\sum_i q_i x_i}{\sum_i q_i} \tag{3.25}$$

$$Y = \frac{\sum_i q_i y_i}{\sum_i q_i}. \tag{3.26}$$

The angular momentum invariant is related to the dispersion of the system:

$$D = \frac{\sum_i q_i \left\{ (X - x_i)^2 + (Y - y_i)^2 \right\}}{\sum_i q_i}. \tag{3.27}$$

The final invariant involves the interaction energy of the system:

$$W = -\frac{1}{4\pi} \sum_i \sum_{j \neq i} q_i q_j \ln r_{ij} \tag{3.28}$$

where r_{ij} is the distance between vortex i and vortex j.

These invariants constitute constraints on the development of a system in the 2d model. In the cases considered in this paper, all the vortices have the same sign. Viecelli (1994) explains how the interplay of the energy and dispersion invariants prevent point-vortices from moving arbitrarily close to each other. As point-vortices near each other, the contribution to the energy invariant from the vortices increases, so all the other vortices in the system must disperse, thus the mean separation of vortices must increase. This process cannot occur indefinitely without violating the dispersion invariant. Therefore, in the initializations considered here, a cloud of like-signed vortices will remain a cloud throughout the development of the model in time. The centroid invariants further determine that the mean position of the cloud of vortices is the same, so we can further expect that none of the point-vortices will travel to infinity.

3.2 Quasi-Geostrophic Shallow Water Point Vortex Model

3.2.1 Analytical Description

The quasi-geostrophic shallow water model (QGSW model) extends these ideas to a weakly divergent model. The QGSW model permits the addition of a size parameter κ which represents the inverse Rossby radius of the fluid. The 2d model is realized when κ vanishes.

The momentum and continuity equations for the shallow water model with beta plane approximation are

$$\frac{\partial u}{\partial t} + u\frac{\partial u}{\partial x} + v\frac{\partial u}{\partial y} - \left[f_0 + \beta\left(y - y_0\right)\right] v = -g\frac{\partial \eta}{\partial x} \tag{3.29}$$

$$\frac{\partial v}{\partial t} + u\frac{\partial v}{\partial x} + v\frac{\partial v}{\partial y} + \left[f_0 + \beta\left(y - y_0\right)\right] u = -g\frac{\partial \eta}{\partial y} \tag{3.30}$$

$$\frac{\partial \eta}{\partial t} + \frac{\partial\left[\left(h_0 + \eta\right) u\right]}{\partial x} + \frac{\partial\left[\left(h_0 + \eta\right) v\right]}{\partial y} = 0 \tag{3.31}$$

where η is a deviation of the fluid surface from its resting height h_0, u is the zonal velocity, v is the meridional velocity, and $f_0 + \beta\left(y - y_0\right)$ is the variable the Coriolis parameter in the beta plane approximation. The relative potential vorticity conservation principle for the f-plane version of the quasi-geostrophic approximation of the shallow water system is

$$\left(\frac{\partial}{\partial t} + u_G\frac{\partial}{\partial x} + v_G\frac{\partial}{\partial y}\right)\left(\nabla^2\psi - \frac{f_0^2}{gh_0}\psi\right) = 0 \tag{3.32}$$

where $\psi = g\eta/f_0$ is the streamfunction and u_G and v_G are the geostrophic wind, $\vec{u}_G = \hat{k} \times \vec{\nabla}\psi$. The quantity

$$\left(\nabla^2\psi - \frac{f_0^2}{gh_0}\psi\right) \tag{3.33}$$

is the potential vorticity for the f-plane, quasi-geostrophic shallow water system.

We apply the point-vortex approximation by contracting the potential vorticity of the system into a finite number of points with infinite value constructed so that the total integrated potential vorticity of the system is still conserved. The geostrophic streamfunction consistent with a single point-vortex with an inverse Rossby radius of $\kappa = f_0/\sqrt{gh_0}$ is

$$\psi = -\frac{q}{2\pi}K_0\left(\kappa r\right) \tag{3.34}$$

where q represents the circulation induced by a shallow water point-vortex at an infinitesmal distance, r is the distance from the vortex, and K_0 is the modified Bessel function of the second kind of zeroth order. Since the quasi-geostrophic invertibility problem is linear, for N point-vortices

$$\psi(x,y) = -\frac{1}{2\pi}\sum_i q_i K_0(\kappa r_{i0}) \tag{3.35}$$

where r_{i0} is the distance from (x,y) to vortex i.

Since a vortex will not advect itself, the development of that vortex is due to the evaluation of ψ due to all the other vortices. The development of vortex i is then described by

$$\frac{\mathrm{d}x_i}{\mathrm{d}t} = -\frac{1}{2\pi}\sum_{j\neq i}\frac{(y_i - y_j)}{r_{ij}} q_j \kappa K_1(\kappa r_{ij}) \tag{3.36}$$

$$\frac{\mathrm{d}y_i}{\mathrm{d}t} = \frac{1}{2\pi}\sum_{j\neq i}\frac{(x_i - x_j)}{r_{ij}} q_j \kappa K_1(\kappa r_{ij}) \tag{3.37}$$

where K_1 is the modified Bessel function of the second kind of first order. This pair of equations is numerically integrated with a fixed-timestep, fourth-order Runge-Kutta scheme in FORTRAN. The Bessel functions are evaluated with series representations (Abramowitz and Stegun, 1972, pp. 255, 258, 375).

$$K_0(z) = -\left[\ln\left(\frac{z}{2}\right) + \gamma\right] + \sum_{m=1}^{\infty}\left[\sum_{n=1}^{m}\frac{1}{n} - \ln\left(\frac{z}{2}\right) - \gamma\right]\frac{\left(\frac{z^2}{4}\right)^m}{(m!)^2} \tag{3.38}$$

where $\gamma \doteq 0.5772$ is the Euler-Mascheroni constant; and

$$K_1(z) = \frac{1}{z} + \frac{z}{4}\sum_{m=0}^{\infty}\left\{\left[2\ln\left(\frac{z}{2}\right) - \psi'(m+1) - \psi'(m+2)\right]\frac{\left(\frac{z^2}{4}\right)^2}{m!\,(m+1)!}\right\} \tag{3.39}$$

where

$$\psi'(n) = -\gamma + \sum_{m=1}^{n-1}\frac{1}{m}. \tag{3.40}$$

These representations sufficiently converge for arguments $z < 10$ when $m \leq 20$.

3.2.2 Non-dimensionalization

As discussed in Section (3.1.2), the equations of motion are non-dimensionalized. For their derivation, begin with the more general continuous field formulation of the x-component forecast equation (3.36)

$$\frac{\mathrm{d}x}{\mathrm{d}t} = -\frac{1}{2\pi}\int \frac{y-y'}{r'}\, q'\kappa\, K_1\left(\kappa r'\right)\, \mathrm{d}A' \tag{3.41}$$

where primed quantities are considered at the source point and r' is the distance from the source point to the observation point. Non-dimensionalizing for the vortex core, consider the radius of maximum winds, R, to be the characteristic length, and define

$$x = x_* R \tag{3.42}$$

$$y = y_* R \tag{3.43}$$

$$y' = y'_* R \tag{3.44}$$

$$r' = r'_* R \tag{3.45}$$

$$\kappa = \frac{\kappa_*}{R} \tag{3.46}$$

where the starred quantities are non-dimensional. Also, define

$$t \equiv t_* T \tag{3.47}$$

where T is a characteristic time scale to be determined below.

Substituting into (3.41)

$$\frac{\mathrm{d}\left(x_* R\right)}{\mathrm{d}\left(t_* T\right)} = -\frac{1}{2\pi}\int \frac{y_* R - y'_* R}{r'_* R}\, q'\frac{\kappa_*}{R}\, K_1\left(\frac{\kappa_*}{R} r'_* R\right)\, \mathrm{d}\left(x'_* R\right)\, \mathrm{d}\left(y'_* R\right) \tag{3.48}$$

and simplifying gives

$$\frac{\mathrm{d}x_*}{\mathrm{d}t_*} = -\frac{T}{2\pi}\int \frac{y_* - y'_*}{r'_*}\, q'\kappa_*\, K_1\left(\kappa_* r'_*\right)\, \mathrm{d}x'_*\, \mathrm{d}y'_*. \tag{3.49}$$

Non-dimensionalize q

$$q' = \frac{q'_*}{T} \tag{3.50}$$

and define T such that the average potential vorticity in the inner core of the storm is unity, $q'_* = 1$. The resulting non-dimensionalized motive equation

$$\frac{\mathrm{d}x_*}{\mathrm{d}t_*} = -\frac{1}{2\pi}\int \frac{y_* - y'_*}{r'_*}\, q'\kappa_*\, K_1\left(\kappa_* r'_*\right)\, \mathrm{d}x'_*\, \mathrm{d}y'_* \tag{3.51}$$

is formally the same as the dimensional motive equation. Discretization follows in the same way as Section (3.2.1). The forecast equation is thus

$$\frac{\mathrm{d}x_{i_*}}{\mathrm{d}t_*} = -\frac{1}{2\pi}\sum_{j\neq i}\frac{y_{i_*} - y_{j_*}}{r_{ij_*}} q_{j_*}\kappa_* K_1(\kappa_* r_{ij_*}). \tag{3.52}$$

The time scale defined here is sufficient for the non-dimensionalization and integration on a computer. For the purposes of interpretation, we felt it was necessary to interpret the system in terms of "circulation time", i.e. the time it takes for the bulk of the system to complete a circuit. In the QGSW model, q_i defines the circulation at an infinitesmal distance away from vortex i. Because there is negative vorticity in the continuous field around the point-vortex, the system can be expected to rotate slower than the 2d model for the same values of q_i. For this reason, the circulation time is diagnosed from the numerical output of the model. The procedure is to define a relaxed period of output, compute an average potential vorticity profile from the relaxed period, invert for the streamfunction, and use the maximum derived geostrophic tangential velocity to compute the circulation time.

3.2.3 Integral Invariants

Like the 2d model (Section 3.1.3), the QGSW model carries with it some invariants. The centroid (linear momentum) invariants and the dispersion (angular momentum) invariant follow along the same lines as the 2d model (3.25 - 3.27)

$$X = \frac{\sum_i q_i x_i}{\sum_i q_i} \tag{3.53}$$

$$Y = \frac{\sum_i q_i y_i}{\sum_i q_i}. \tag{3.54}$$

$$D = \frac{\sum_i q_i \left\{ (X - x_i)^2 + (Y - y_i)^2 \right\}}{\sum_i q_i}. \tag{3.55}$$

where now q is defined from the potential vorticity rather than vorticity. The energy invariant is

$$W = \frac{1}{4\pi} \sum_i \sum_{j \neq i} q_i q_j \, K_0 \left(\kappa r_{ij} \right) \tag{3.56}$$

where r_{ij} is the distance between the points i and j. These invariants behave in much the same way as in the 2d model. Again we can rely on the concepts that point-vortices of the same sign will remain in a cloud and will not travel to infinity. Because the Green's function for this case vanishes exponentially with increasing distance, the terms at infinity vanish. Again, the invariants have been divided by the total circulation invariant to provide geometrical insight.

Chapter 4

THE PROBLEM OF VORTICITY RELAXATION

The approach of this chapter is to examine the relaxation of an unstable vortex. Harkening back to the discussion in Chapter 1 (Figures 1.1 - 1.3), the flavor of the approach here is to approximate the observed vorticity distribution in the inner core of a hurricane with a three-region step-function in vorticity profile, discretized with a finite number of point-vortices. The parameters are chosen so that the numerical simulation evolves in a way that is largely axisymmetric. This is done to study only limited aspects of the response of an unstable vortex system, and because such an approach lends itself to axisymmetric analysis. This by no means minimizes the importance of a non-axisymmetric evolution. A significant and observable non-axisymmetric response evolves with proper selection of parameters, but such a system cannot be completely described by the simple objective analysis techniques described below.

4.1 Initializations

The advective relaxation of the unstable, barotropic vortex is examined using a family of initializations that are variations on a basic theme, that the vorticity in the center of the vortex is lower than the vorticity in an exterior region. This is represented conceptually by a step function in the radial profile.

Individual point-vortices are allocated in one of two ways. The first is to use point-vortices with equal strengths. Then the number of point-vortices are allocated between the two regions according to the total circulation of each region. The spacing between the points in each of the regions is initially different. The second method is to vary the vortex strengths between the two regions, spacing the vortices throughout the vortex cloud evenly. The numbers of vortices allocated to each region is then determined by the

relative areas of the regions. Experiments initialized with variable vortex densities (the first method above) will be designated hereafter as `dense`. Experiments initialized with variable vortex strengths (the second method above) will be designated hereafter as `vorts`. Table (4.1) summarizes the different simulations. As an example, the spatial arrangement of the 360 equal strength vortices for the `Qdense2` initialization is shown in Figure (4.1), while Figure (4.2) shows the spatial arrangement for the `Qvorts2` initialization. The 180 vortices marked by an "X" have twice the circulation of the 180 vortices marked by a "+".

As discussed in Chapter 3, the 2d model experiments are conducted with a nondimensionalized total circulation of π and a nondimensional maximum radius of unity. In the 2d model, the discretization of the vorticity field by the point-vortices produces the desired arrangement of the circulation (the area integral of vorticity). In QGSW model, the discretization of the potential vorticity field by the point-vortices produces the desired arrangement of the area integral of potential vorticity. Thus, q in the 2d model represents the circulation of the point-vortex; q in the QGSW model represents the area integral of potential vorticity of the point-vortex. Hereafter, if there is no distinction between the 2d model and the QGSW model, potential vorticity may be referred to in the description of an analysis scheme; in practice, vorticity is substituted for analysis in the 2d model.

The initialized distribution of the radial positions of the point-vortices in the `dense2`, `Ddense2`, `Qdense2`, `vorts2`, `Dvorts2`, and `Qvorts2` simulations is designed to emulate the vorticity profile shown in Figure (4.3). The same is shown in Figure (4.4) for the `Qdense3`, `vorts3`, and `Qvorts3` simulations, and in Figure (4.7) for the `Qdenseemily` simulation, Figure (4.5) for the `Qdense2W` simulation, and Figure (4.6) for the `Qdense3W` simulation.

The initialized distribution of the radial positions of the point-vortices in the `b1.0dense2`, `b1.0Qdense2`, `b1.0vorts2`, and `b1.0Qvorts2` simulations are designed to emulate the potential vorticity profile shown in Figure (4.8). The same is shown in Figure (4.9) for the `b1.0Qdense3` simulation, in Figure (4.10) for the `b1.0Qdense2W` simulation, and in Figure (4.11) for the `b1.0Qdense3W` simulation. The tangential velocity and vorticity profiles are also shown. The same may be shown for the initializations for QGSW model runs with an inverse Rossby radius of 0.1, but since this case nearly models the 2d

simulation name	N	vorticity	area	(Rossby radius)$^{-1}$
dense2	90	2.0	0.5	2d
Ddense2	180	2.0	0.5	2d
Qdense2	360	2.0	0.5	2d
vorts2	90	2.0	0.5	2d
Dvorts2	180	2.0	0.5	2d
Qvorts2	360	2.0	0.5	2d
Qdense3	360	3.0	0.5	2d
Qdenseemily	360	3.057	5.340	2d
vorts3	90	3.0	0.5	2d
Qvorts3	360	3.0	0.5	2d
Qdense2W	360	2.0	1.0	2d
Qdense3W	360	3.0	1.0	2d
Qtophat	360	1.0	N/A	2d
Otophat	720	1.0	N/A	2d
Qdensestable	360	N/A	3.938	2d
b0.1dense2	90	2.0	0.5	0.1
b0.1Qdense2	360	2.0	0.5	0.1
b0.1vorts2	90	2.0	0.5	0.1
b0.1Qvorts2	360	2.0	0.5	0.1
b1.0dense2	90	2.0	0.5	1.0
b1.0Qdense2	360	2.0	0.5	1.0
b1.0vorts2	90	2.0	0.5	1.0
b1.0Qvorts2	360	2.0	0.5	1.0
b1.0Qdense3	360	3.0	0.5	1.0
b1.0Qdense2W	360	2.0	1.0	1.0
b1.0Qdense3W	360	3.0	1.0	1.0

Table 4.1: The parameters specified for each of the simulations referred to in this paper. Simulation names containing the string `dense` refer to those simulations where variations in vortex spacings produce differences in the continuous analog of the potential vorticity field. Simulation names containing the string `vorts` refer to those simulations where variations in vortex strengths produce differences in the continuous analog of the potential vorticity field. N is the number of vortices in the simulation. The "vorticity" column refers to the ratio of potential vorticity in the exterior region over that of the interior region. The "area" column refers to the ratio in area between the exterior region over that of the interior region. The inverse Rossby radius is referred to in non-dimensional inverse length units. See Section (3.2.2) for further details.

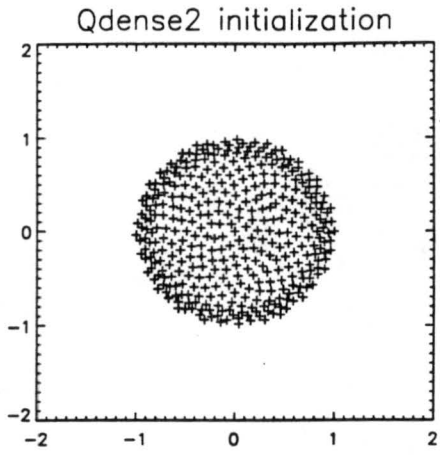

Figure 4.1: Initial distribution of vortices in the `Qdense2` simulation.

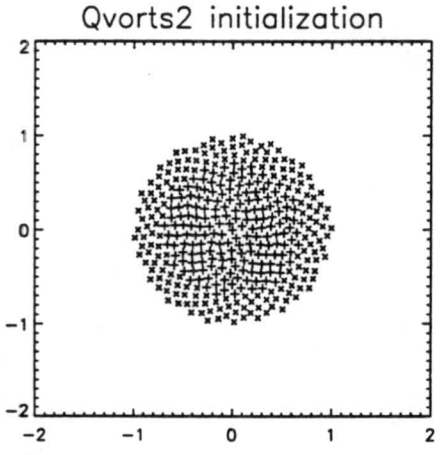

Figure 4.2: Initial distribution of vortices in the `Qvorts2` simulation. Vortices marked by an "X" have twice the circulation of those marked by a "+".

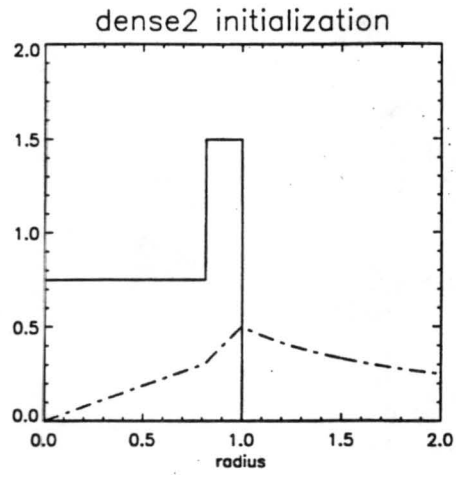

Figure 4.3: Profiles of the initial state vorticity (solid) and tangential velocity (dashed) for the **dense2** simulation.

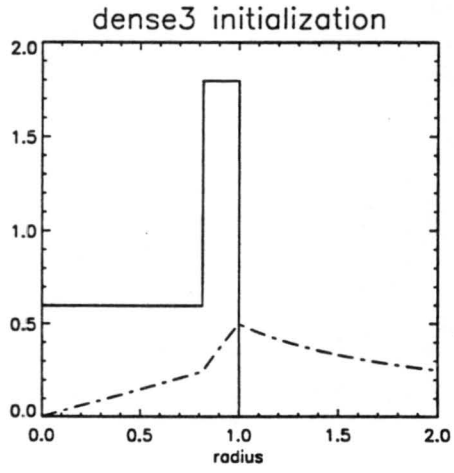

Figure 4.4: Profiles of the initial state vorticity (solid) and tangential velocity (dashed) for the **dense3** simulation.

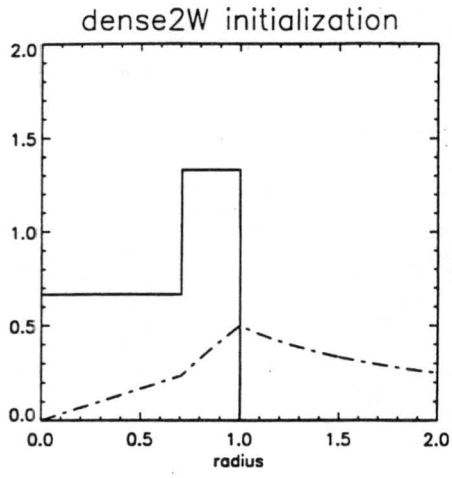

Figure 4.5: Profiles of the initial state vorticity (solid) and tangential velocity (dashed) for the **dense2W** simulation.

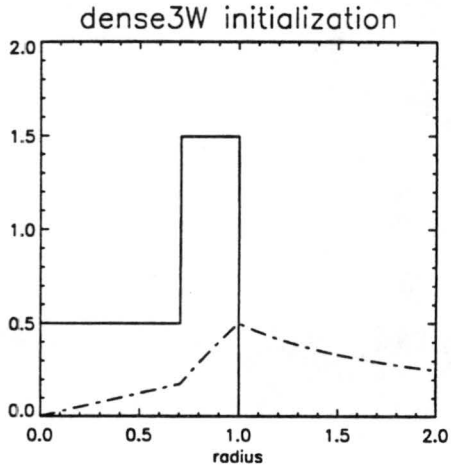

Figure 4.6: Profiles of the initial state vorticity (solid) and tangential velocity (dashed) for the **dense3W** simulation.

model, the vorticity curve is nearly indistinguishable from the potential vorticity curve. In these cases, the reader is referred to Figure (4.3).

4.2 Relaxed State

Methods for describing the spatial potential vorticity distribution in the (x, y)-plane from point-vortex model output are not entirely satisfactory. While we can gain good intuitive understanding of the processes involved in filamentation of an ellipse (Figure 1.4) or the merger of identical vortices (Figures 1.5, 1.6) from visual inspection of the distribution of the vortex cloud, detailed understanding of the relaxation process in the interior of the vortex cloud must take advantage of subtleties in point-vortex strengths and spacings. In order to characterize the potential vorticity field, profiling techniques are used. By removing a degree of freedom from the analysis, the density of information is increased in the remaining dimension and the data can be considered statistically. In this way, the relaxed state (and the current state) of the system can be characterized.

In determining what the relaxed state is for a given model simulation, it is necessary to take advantage of a tautology; that after the system has achieved the relaxed state, the system will maintain the character of the relaxed state. Further, it is assumed that relaxation occurs fairly quickly, thus the relaxed state will be captured in a simulation of finite length. It is shown below in Section (4.3) that a quantity can be constructed to characterize the degree of correlation to a relaxed state and that it converges quickly. Then, we can conclude that we can identify the relaxed state, and can identify characteristics of that state.

Observation of the relaxed state of the system suggest that a time average of potential vorticity contains the same character as a spatial average; thus the relaxed state exhibits ergodic behavior. Since potential vorticity is the most primitive variable of output from the model, we will begin with the characterization of the relaxed vortex through time averages of the potential vorticity. Axisymmetry of the relaxed state is assumed, so the character of radial profiles are considered. A fine mesh of radial bins are used to represent the profile. At each time step, if a vortex is found in a bin, then the strength of the vortex

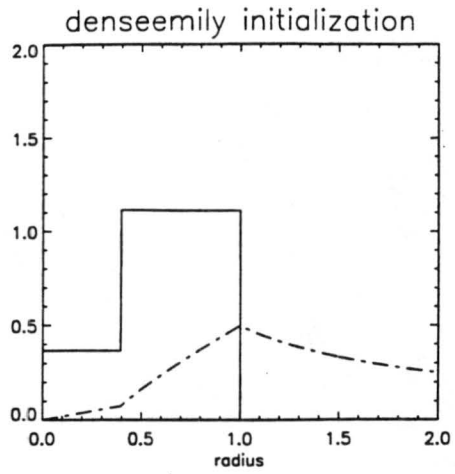

Figure 4.7: Profiles of the initial state vorticity (solid) and tangential velocity (dashed) for the `denseemily` simulation.

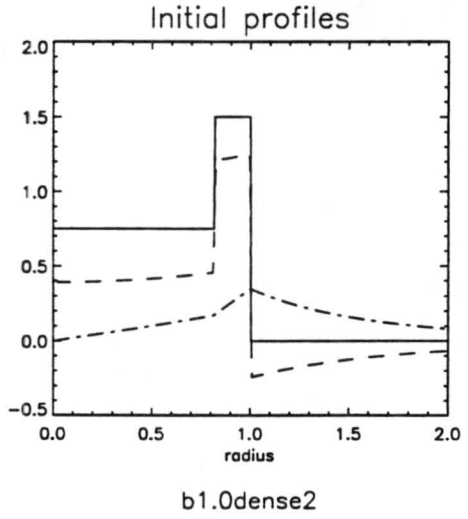

Figure 4.8: Profiles of the initial state potential vorticity (solid), vorticity (dashed) and tangential velocity (dash-dotted) for the `b1.0dense2` simulation.

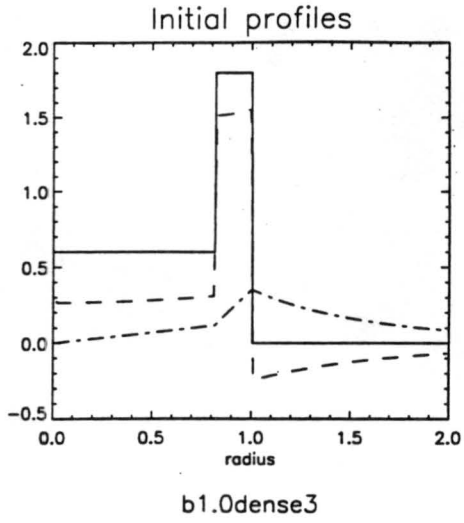

Figure 4.9: Profiles of the initial state potential vorticity (solid), vorticity (dashed) and tangential velocity (dash-dotted) for the `b1.0dense3` simulation.

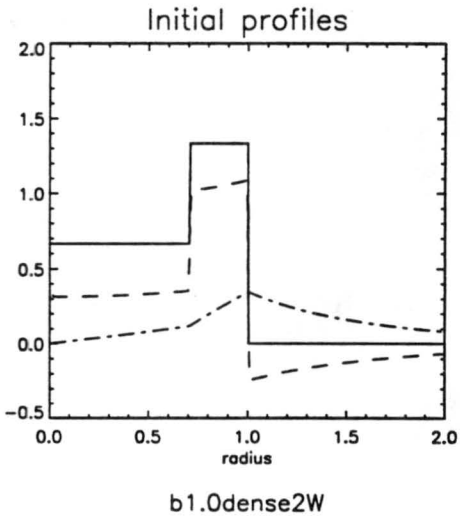

Figure 4.10: Profiles of the initial state potential vorticity (solid), vorticity (dashed) and tangential velocity (dash-dotted) for the `b1.0dense2W` simulation.

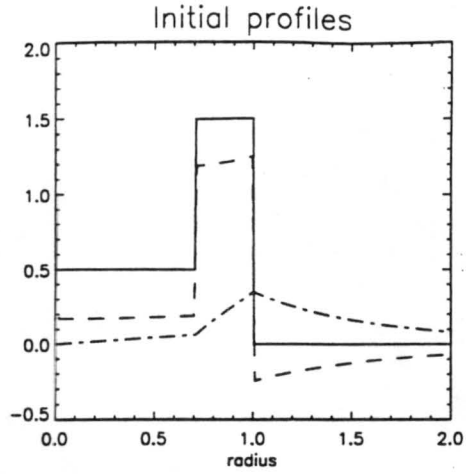

Figure 4.11: Profiles of the initial state potential vorticity (solid), vorticity (dashed) and tangential velocity (dash-dotted) for the `b1.0dense3W` simulation.

is augmented to that bin. This is performed for every time step that has been determined to represent the relaxed state. Then the value of each bin is divided by the total number of time steps analyzed and by the area represented by the bin. The central bin has an area of $\pi\,(\delta r)^2$. The other bins have area $2\pi r\delta r$, and their mean potential vorticity may be described by

$$\bar{P}(r) = \frac{1}{T \cdot 2\pi r \delta r} \sum_{t=1}^{T} \sum_{k=1}^{K} q_{t,k} \tag{4.1}$$

where $q_{t,k}$ is the strength of the k-th vortex that lies in the shell $(r, r+\delta r)$ at the t-th time step, N is the number of vortices that lie in the shell at that time, and T is the number of time steps for analysis.

4.2.1 2d model

In the case of the 2d model, the vorticity profile is computed. The tangential wind field can be computed with the use of Stoke's Theorem

$$\iint_A \vec{\zeta} \cdot \hat{n}\, \mathrm{d}A = \oint_C \vec{v} \cdot \mathrm{d}\hat{s} \tag{4.2}$$

where $\hat{n}$ is a unit vector normal to A, an area for consideration, bounded by a contour C, $\vec{\zeta}$ is the vorticity and $\mathrm{d}\hat{s}$ is a unit vector of integration that is locally tangent to C. Considering only a two-dimensional plane

$$\iint_A \zeta\, \mathrm{d}A = \oint_C \vec{v} \cdot \mathrm{d}\hat{s} \tag{4.3}$$

and then considering the area A to be a circle and that ζ is symmetrically distributed, (4.3) simplifies

$$2\pi \int_0^r \zeta r' \, \mathrm{d}r' = 2\pi r v_{\mathrm{tan}} \tag{4.4}$$

thus the velocity tangent to the circle is

$$v_{\mathrm{tan}}(r) = \frac{1}{r} \int_0^r \zeta r' \, \mathrm{d}r' \tag{4.5}$$

in the 2d model.

4.2.2 QGSW model

In order to determine the mean streamfunction from a given profile in potential vorticity in the QGSW model, it is necessary to solve the following invertibility problem for $\bar{\psi}(r)$:

$$\frac{\mathrm{d}^2\bar{\psi}(r)}{\mathrm{d}r^2} + \frac{1}{r}\frac{\mathrm{d}\bar{\psi}(r)}{\mathrm{d}r} - \kappa^2\bar{\psi}(r) = \bar{q}(r) \tag{4.6}$$

where $\bar{\psi}(r = 0)$ is finite and $\mathrm{d}\bar{\psi}/\mathrm{d}r$ vanishes as $r \to \infty$. A Green's function method is used here to solve (4.6). Once the streamfunction is found, the tangential velocity and vorticity are deduced from

$$\bar{v}_{\mathrm{tan}} = \frac{\mathrm{d}\bar{\psi}}{\mathrm{d}r} \tag{4.7}$$

and

$$\bar{\zeta} = \frac{\bar{v}_{\mathrm{tan}}}{r} + \frac{\mathrm{d}\bar{v}_{\mathrm{tan}}}{\mathrm{d}r}. \tag{4.8}$$

First, we write the differential equation (4.6) in a canonical form

$$\frac{\mathrm{d}}{\mathrm{d}r}\left(r\frac{\mathrm{d}\bar{\psi}}{\mathrm{d}r}\right) - \kappa^2 r\bar{\psi} = \bar{q}r. \tag{4.9}$$

Replace the right hand side of Equation (4.9) with a one-dimensional Dirac delta function constructed such that

$$\int_{\rho-\varepsilon}^{\rho+\varepsilon} \delta(r-\rho)\, \mathrm{d}r = 1. \tag{4.10}$$

The Green's function problem is then defined by

$$\frac{\mathrm{d}}{\mathrm{d}r}\left(r\frac{\mathrm{d}G}{\mathrm{d}r}\right) - \kappa^2 rG = \delta(r-\rho). \tag{4.11}$$

The homogeneous form of (4.11) is Bessel's modified equation of zero order. Two linearly independent solutions are given by $I_0(\kappa r)$ and $K_0(\kappa r)$. I_0 grows exponentially for large argument, and K_0 is logarithmically singular for small argument. I_0 is bounded for small argument, and K_0 is bounded for large argument. To satisfy the boundary conditions on $\bar{\psi}(r)$, the I_0 solution is applied as the solution when r is less than ρ, and K_0 is applied at large argument, thus

$$G(r,\rho) = \begin{cases} C_1 I_0(\kappa r) & ; \quad r \leq \rho \\ C_2 K_0(\kappa r) & ; \quad r \geq \rho \end{cases} \tag{4.12}$$

where C_1 and C_2 are yet to be determined. Since we know $\bar{\psi}$ must be continuous, impose continuity on G across ρ, giving

$$\lim_{r \to \rho^+} G(r,\rho) = \lim_{r \to \rho^-} G(r,\rho) \tag{4.13}$$

thus

$$C_2 K_0(\kappa\rho) = C_1 I_0(\kappa\rho). \tag{4.14}$$

By integrating the Green's function equation (4.11) over a small interval containing ρ, we note that the second term on the left hand side vanishes because the integrated quantity is finite, while the first term immediately integrates to

$$\left.\frac{dG}{dr}\right]_{r=\rho^-}^{r=\rho^+} = \frac{1}{\rho}. \tag{4.15}$$

Substituting (4.12) into (4.15) gives

$$C_2 \kappa K_0'(\kappa\rho) - C_1 \kappa I_0'(\kappa\rho) = \frac{1}{\rho} \tag{4.16}$$

where primes denotes differentiation with respect to the argument. The continuity condition (4.14) then yields

$$\frac{C_1 \kappa\rho}{K_0(\kappa\rho)} \left\{ I_0(\kappa\rho)\ K_0'(\kappa\rho) - I_0'(\kappa\rho)\ K_0(\kappa\rho) \right\} = 1. \tag{4.17}$$

Based on the series representation of I_0 and K_0 for small z can show that the Wronskian

$$W(I_0, K_0; z) = I_0(z) K_0'(z) - I_0'(z) K_0(z) \tag{4.18}$$

is simply

$$W = -\frac{1}{z}. \tag{4.19}$$

Equation (4.17) then determines

$$\begin{aligned} C_1 &= \frac{K_0(\kappa\rho)}{\kappa\rho\{I_0(\kappa\rho)K_0'(\kappa\rho) - I_0'(\kappa\rho)K_0(\kappa\rho)\}} \\ &= -\frac{K_0(\kappa\rho)}{\kappa\rho W(\kappa\rho)} \\ &= -K_0(\kappa\rho); \end{aligned} \tag{4.20}$$

and (4.14) gives

$$C_2 = -I_0(\kappa\rho). \tag{4.21}$$

The derived Green's function is thus

$$G(r,\rho) = \begin{cases} -K_0(\kappa\rho)I_0(\kappa r) & ; \quad r \le \rho \\ -I_0(\kappa\rho)K_0(\kappa r) & ; \quad r \ge \rho \end{cases}. \tag{4.22}$$

The streamfunction then follows by forming $\int [G \cdot (4.6) - \bar{\psi}(4.11)]\,\mathrm{d}r$ and invoking the boundary conditions:

$$\bar{\psi}(r) = \int_0^\infty G(r,\rho)\,\rho\bar{q}(\rho)\,\mathrm{d}\rho. \tag{4.23}$$

4.2.3 Comparison

Comparison of the relaxed states resulting from the different simulations shows sensitivity to the initial state, but also affirms notions regarding the stability of vortices, namely the Raleigh's stability criterion (Gent and McWilliams, 1986). The 360 vortex runs are shown in Figures (4.12 - 4.21). Appendix A demonstrates the independence of the relaxed state to vortex number and arrangement.

The relaxed profiles of vorticity in the `Qdense2` simulation is more top-hatted than the monopolar relaxed state of the `Qdense3` simulation. The top-hat (Rankine-like) profile of the `Qdense2` simulation shows a nearly constant value of vorticity between the center and $r = 1$, with a slight peak near the center and a smooth tail at $r > 1$. The relaxed states for the `Qdense2W` and `Qdense3W` simulations are respectively quite like the `Qdense2` and `Qdense3` simulations, but the `Qdense2W` relaxed state suggests more a monopolar profile, with a larger central peak and tail. The relaxed state for `Qdenseemily` has a mixed

simulation	δ	$v_{\tan}(\delta)$	wave	e-folding time
`Qdense2`	0.816497	0.612372	7	2.7524
			8	0.9466
			9	0.9304
			10	2.5537
`Qdense3`	0.816497	0.489898	5	0.8576
			6	0.5042
			7	0.4665
			8	0.5840
`Qdense2W`	0.707107	0.471405	6	1.3505
`Qdense3W`	0.707107	0.353553	4	0.9003
			5	0.7351
`Qdenseemily`	0.397151	0.145341	3	2.8723

Table 4.2: Analysis of the exponential growth rates of unstable linear modes for the initializations 2d model simulations (Michalke and Timme, 1967; see Section 2.2). The "δ" column is the radius of the jump in vorticity between the two regions. The "$v_{\tan}(\delta)$" column is listed as per the non-dimensionalization of Michalke and Timme, and is double the non-dimensionalized tangential velocity depicted in the figures in this chapter. The "wave" column refers to mode of all exponentially growing modes that result from the analysis, with corresponding e-folding times listed in terms of circuit period in the "e-folding time" column.

top-hat/monopolar character. Since the top-hat profile represents a relaxed state, it is proposed that `Qdense2` and `Qdense2W` relaxed to such a profile simply because the initializations are fairly similar to the top-hat profile. A stability analysis based on the technique of Michalke and Timme (1967) (Table 4.2) suggests that the `Qdense3` and `Qdense3W` initializations are more unstable than, respectively, the `Qdense2` and `Qdense2W` initializations. The more unstable cases also show instability in lower wavenumbers.

The QGSW model simulations with values of the inverse Rossby radius of 0.1 are very similar to the 2d model runs, since in the 2d model case, the inverse Rossby radius vanishes.

The QGSW model simulations with values of the inverse Rossby radius of 1.0 show qualitatively different character. Comparing the potential vorticity profiles in the QGSW model with the vorticity profiles in the 2d model, the `b1.0Qdense2` simulation has a more monopolar relaxed state than the `Qdense2` simulation, while the `b1.0Qdense3` and `b1.0Qdense3W` relaxed states show much the same character of their 2d model analogs,

which were already fairly monopolar. The inverse Rossby radius reduces the influence of distant vortices upon a particular vortex, and so more local mixing is allowed. The top-hat relaxation can be attributed to the large scale stabilizing influence of the shear in the vortex, which in that case may be more important than any local-scale perturbations related in the instabilities of the system. As the local-scale perturbation becomes more important, the vortices in the perturbation find radial positions that are more scattered inward and outward from the radius of the perturbation. This leads to the more monopolar profiles, which also represent stable states.

The tangential velocity in the top-hat relaxed state is stronger than in the monopolar relaxed states. This maximum is more confined in the top-hat relaxed states, with the monopolar relaxed states showing moderate tangential winds speeds in a broad range of radii.

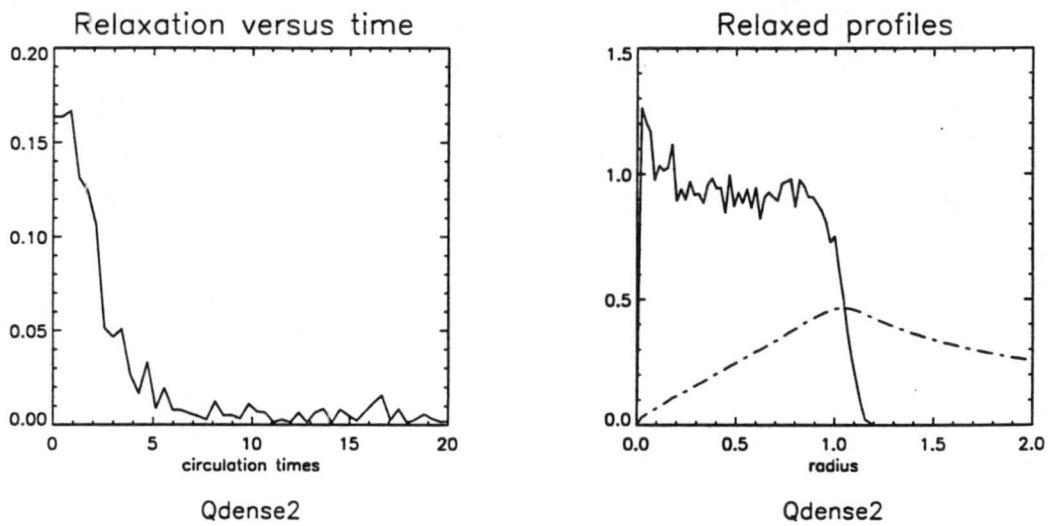

Figure 4.12: (a) Time series of the bin-computed relaxation parameters for the `Qdense2` simulation and (b) profiles of the relaxed state vorticity (solid) and tangential velocity (dashed).

4.3 Relaxation Time

The guiding concept used in determining the relaxation time of the system is to compare the instantaneous state of the system with the relaxed state. To achieve a numerical expression of this statement it is necessary to determine the period of the model run that

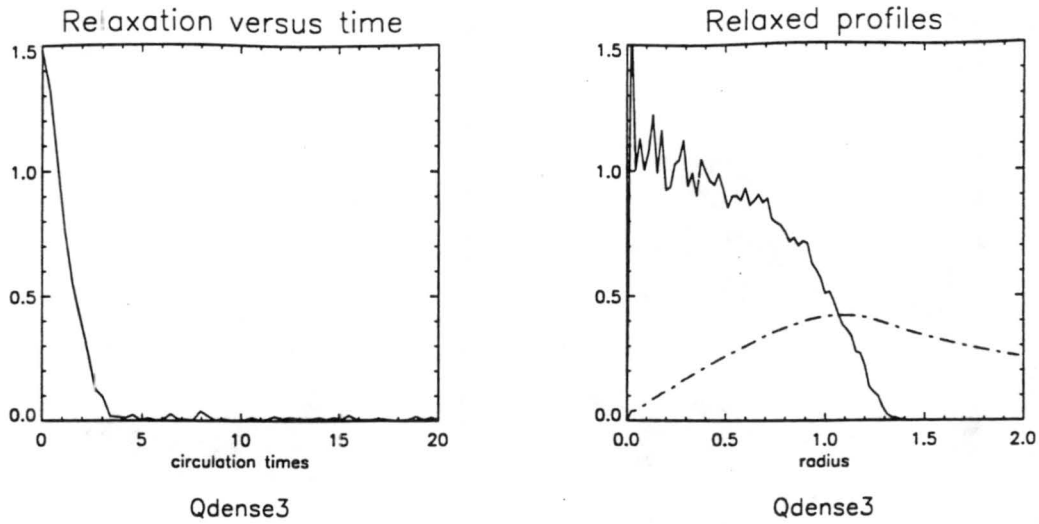

Figure 4.13: (a) Time series of the bin-computed relaxation parameters for the `Qdense3` simulation and (b) profiles of the relaxed state vorticity (solid) and tangential velocity (dashed).

is representative of a relaxed state and to determine a numerical measure of the current (and relaxed) state of the system.

An examination of vorticity profiles at various times in different runs had given the impression that every simulation considered here had reached a relaxed state for a standard length of run, and that the relaxed state is achieved before half the run. For these analyses, the last third of the run is considered relaxed. This period of record is shown in Figure (4.22) to have little effect in the results when compared to other, shorter representative relaxed periods.

The approach is a bin method which compares the radial profiles of potential vorticity with profiles of the relaxed state. Potential vorticity is the natural selection for comparison because it is the most primitive output of the model, which along with position, is a complete description of the current state of the system. The first step is to condense the cartesian positions of the vortices into radial positions (the angular positions are neglected in this profiling technique) from an origin defined by the centroid invariant. One can define a set of bins to group the vortices according to radial intervals, and define a set of these bins for each time step of the model. For the purposes of this analysis, I use four bins and define each bin to represent an equal amount of area in two-dimensional space with the use of a quadratic relation. The outer-most edge of the outer-most bin is defined to be the

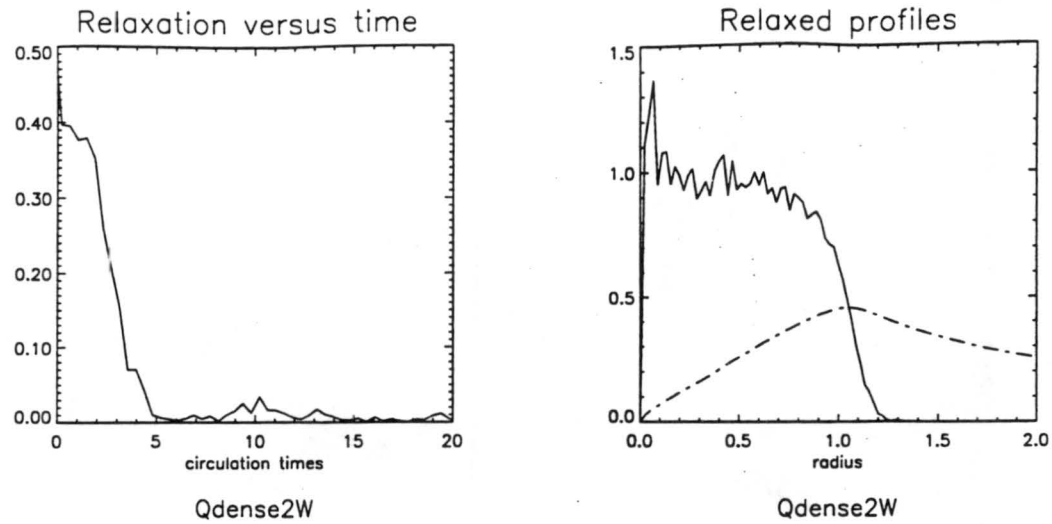

Figure 4.14: (a) Time series of the bin-computed relaxation parameters for the `Qdense2W` simulation and (b) profiles of the relaxed state vorticity (solid) and tangential velocity (dashed).

furthest radial position ever achieved by any vortex at any time in the simulation. Each bin contains the sum total of potential vorticity within that particular radial interval at that particular time. The comparison composite is constructed by averaging these bins over the time interval specified. This is much like (4.24), if r is simply refined as the square of the radius. Since each bin represents the same area, the area is not divided, and only a relative measure is sought, thus the comparison composite for shell j is

$$\bar{P}_j = \frac{1}{T} \sum_{t=1}^{T} \sum_{k=1}^{K} q_{t,k} \tag{4.24}$$

where $q_{t,k}$ is the strength of the k-th vortex that lies in the shell j at the t-th time step, K is the number of vortices that lie in the shell at that time, and T is the number of time steps for analysis.

The sum square of the difference between the bins at a given time and the comparison composite constitutes the numerical measure of relaxation of the system

$$C = \sum_{j=1}^{4} \sum_{k=1}^{K} (q_{t,k} - \bar{P}_j)^2 \tag{4.25}$$

where j indexes the four bins and C is the measure of "relaxation". Small values of C represent a high degree of correlation to the relaxed state. The time of relaxation is considered to be that time when this measure acquires the character of last third of

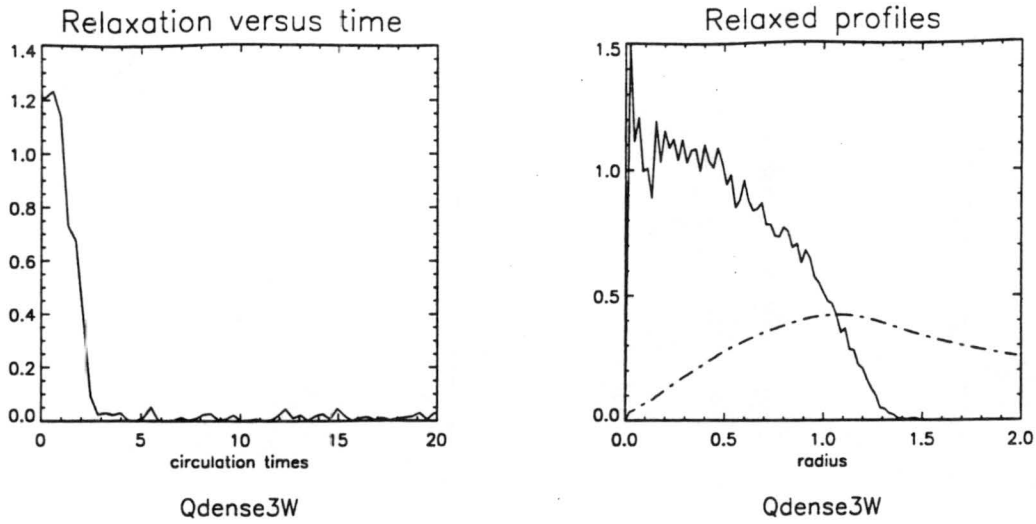

Figure 4.15: (a) Time series of the bin-computed relaxation parameters for the `Qdense3W` simulation and (b) profiles of the relaxed state vorticity (solid) and tangential velocity (dashed).

the simulation. The magnitude of the relaxation parameter, as is evident in the results presented here (Figures 4.12 - 4.21), varies greatly between model runs. The differences between the `Qdense2` and `Qdense3W` simulations are exemplary. The magnitudes of the relaxation parameter vary by an order of magnitude at initialization between the two models. The `Qdense3W` simulation shows a prominent tail in the relaxed vorticity profile, that extends to $\sim$ 1.5 radial units, compared with $\sim$ 1.2 radial units in the `Qdense2` simulation. (In a two-dimensional representation of the locations of the point-vortices, the "tail" is evident as a gradual decrease in density in the point-vortices, which do not appear to exhibit any apparent structure.) The outer-most of the four bins for analysis in the `Qdense3W` simulation is roughly $1.3 < r < 1.5$ and the next bin is $1.06 < r < 1.3$. At initialization, these two bins are empty, so the comparison measure will compare nothing with something, and will compute a rather large sum square difference. In the `Qdense2` simulation, only one outer bin is empty, thus more subtle changes in the vortex are taken advantage of by the relaxation parameter. The different behavior between simulations may not be entirely satisfactory, but we feel that the figures demonstrate the utility of this objective technique. Variations of parameters in the analysis (notably the number of bins and defining the bins by equal areas) show differences primarily in the level of noise

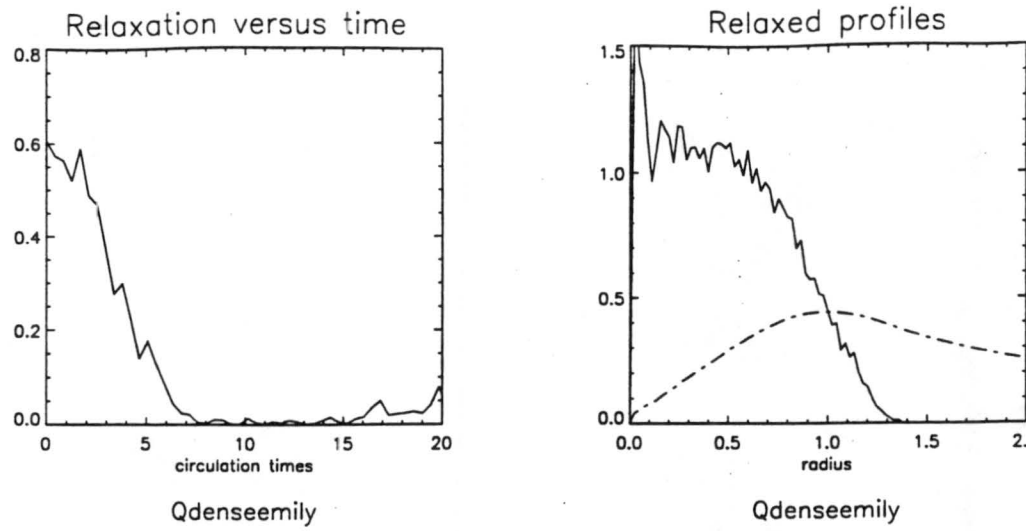

Figure 4.16: (a) Time series of the bin-computed relaxation parameters for the `Qdenseemily` simulation and (b) profiles of the relaxed state vorticity (solid) and tangential velocity (dashed).

in the relaxed state, and the method presented shows the best performance for widest variety of simulations.

In trying to characterize the relaxation time from the results presented in Figures (4.12 - 4.21), the approach used here is to subjectively determine when the relaxation parameter obtains the character of the later part of the simulation. This analysis could be considered accurate to the nearest circulation period. The results of such an analysis are shown in Table (4.3) below.

In each case, the simulations with a large inverse Rossby radius (1.0) relax more quickly than those simulations with a smaller inverse Rossby radius (0.1), and those more quickly than the non-divergent cases. The relaxation occurs due to local scale effects. The QGSW model system rotates at a slower rate, and thus more vortex/vortex interactions may occur during a circuit period. Additionally, the shear in the 2d model vortex establishes a stabilizing influence on particles in the vortex.

There is some correlation between in the relaxation time in the 2d model runs and the linear stability analysis (Table 4.2). Simulations with larger exponential growth rates generally show faster relaxation. The exceptions are the `Qdense2W` and `Qdense3W` simulations, which relax more quickly than their narrow counterparts (`Qdense2` and `Qdense3`,

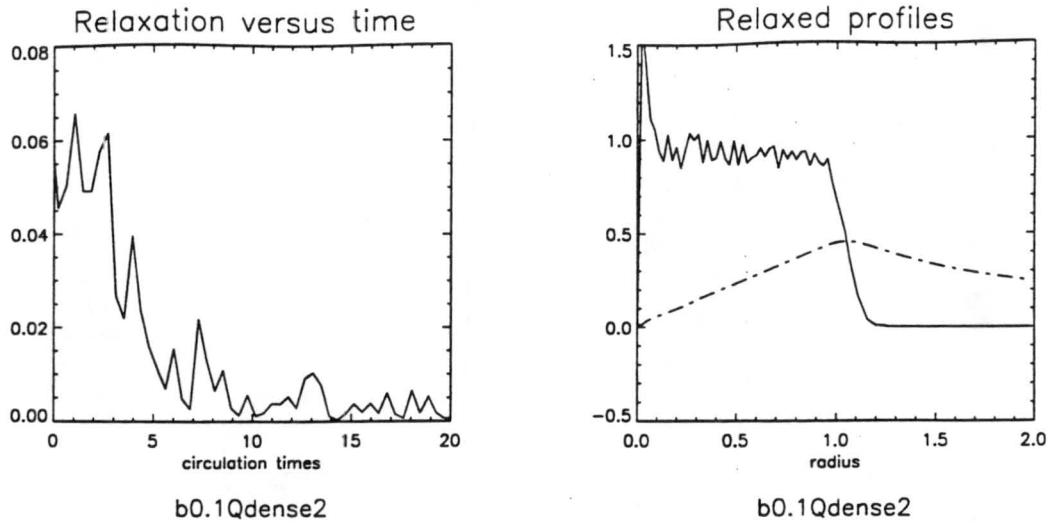

Figure 4.17: (a) Time series of the bin-computed relaxation parameters for the `b0.1Qdense2` simulation and (b) profiles of the relaxed state potential vorticity (solid) and tangential velocity (dashed).

respectively), but we might note that with these cases, lower wavenumbers are more unstable and also that these cases have more prominent tails in their relaxed states. There is no overt evidence in the two-dimensional fields for important wavenumber processes in the relaxation in any of the cases presented in this chapter (for a distinctly asymmetric response, see Appendix D), though, and the lengthing in the circulation time due to the weaker wind speeds is on the order of 1%, so both explanations can probably be dismissed.

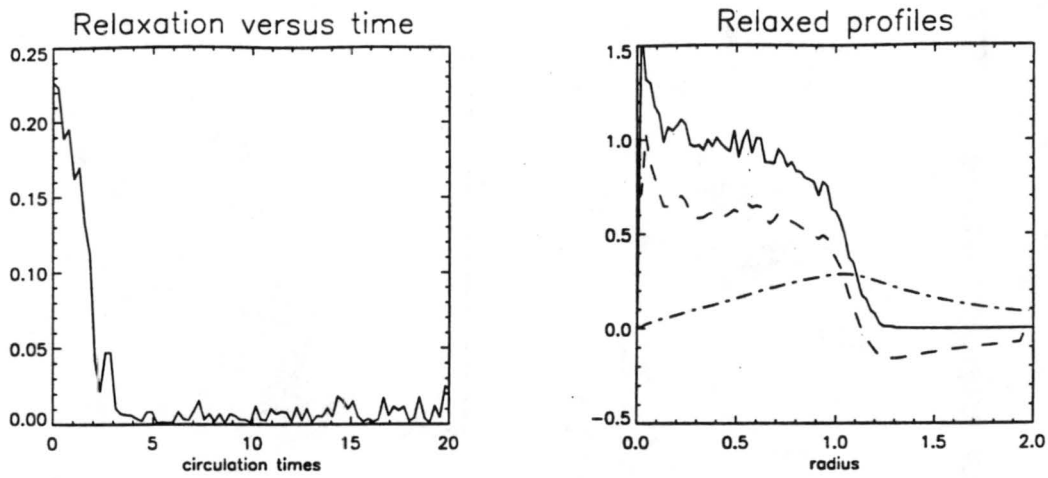

Figure 4.18: (a) Time series of the bin-computed relaxation parameters for the `b1.0Qdense2` simulation and (b) profiles of the relaxed state potential vorticity (solid), vorticity (dashed), and tangential velocity (dash-dotted).

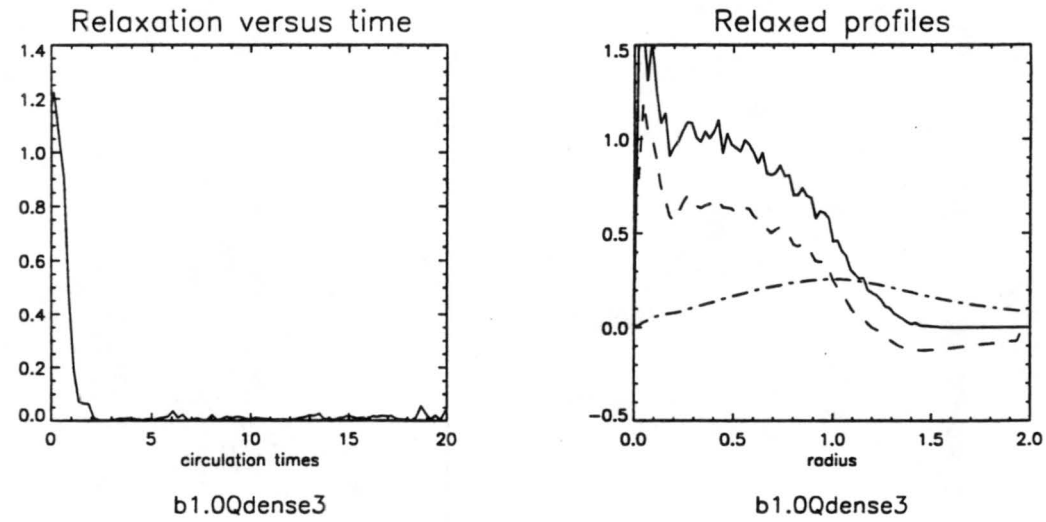

Figure 4.19: (a) Time series of the bin-computed relaxation parameters for the `b1.0Qdense3` simulation and (b) profiles of the relaxed state potential vorticity (solid), vorticity (dashed), and tangential velocity (dash-dotted).

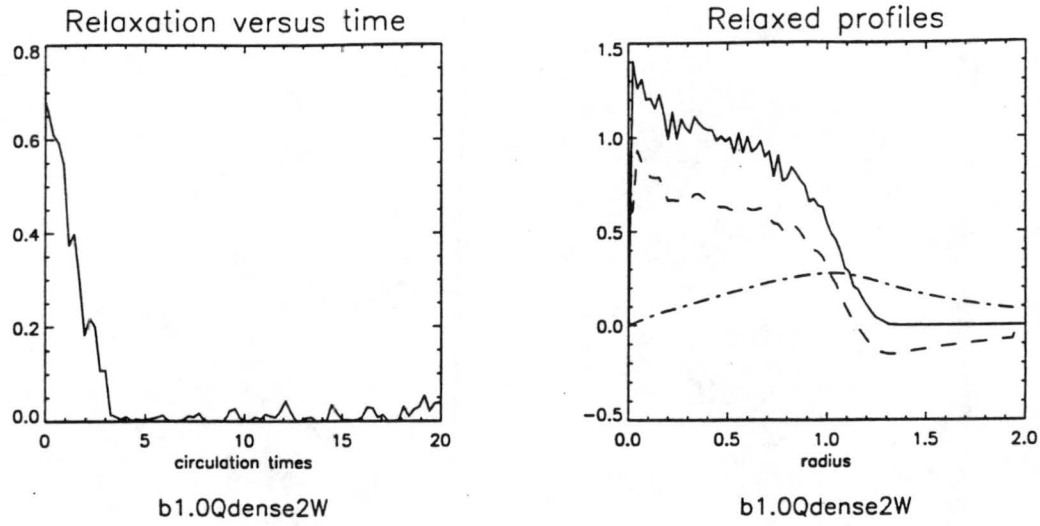

Figure 4.20: (a) Time series of the bin-computed relaxation parameters for the `b1.0Qdense2W` simulation and (b) profiles of the relaxed state potential vorticity (solid), vorticity (dashed), and tangential velocity (dash-dotted).

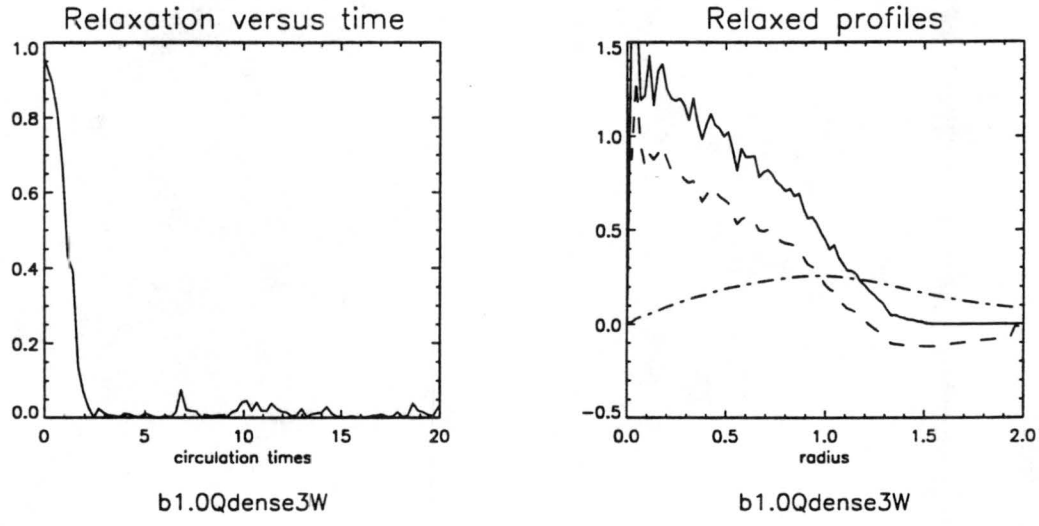

Figure 4.21: (a) Time series of the bin-computed relaxation parameters for the `b1.0Qdense3W` simulation and (b) profiles of the relaxed state potential vorticity (solid), vorticity (dashed), and tangential velocity (dash-dotted).

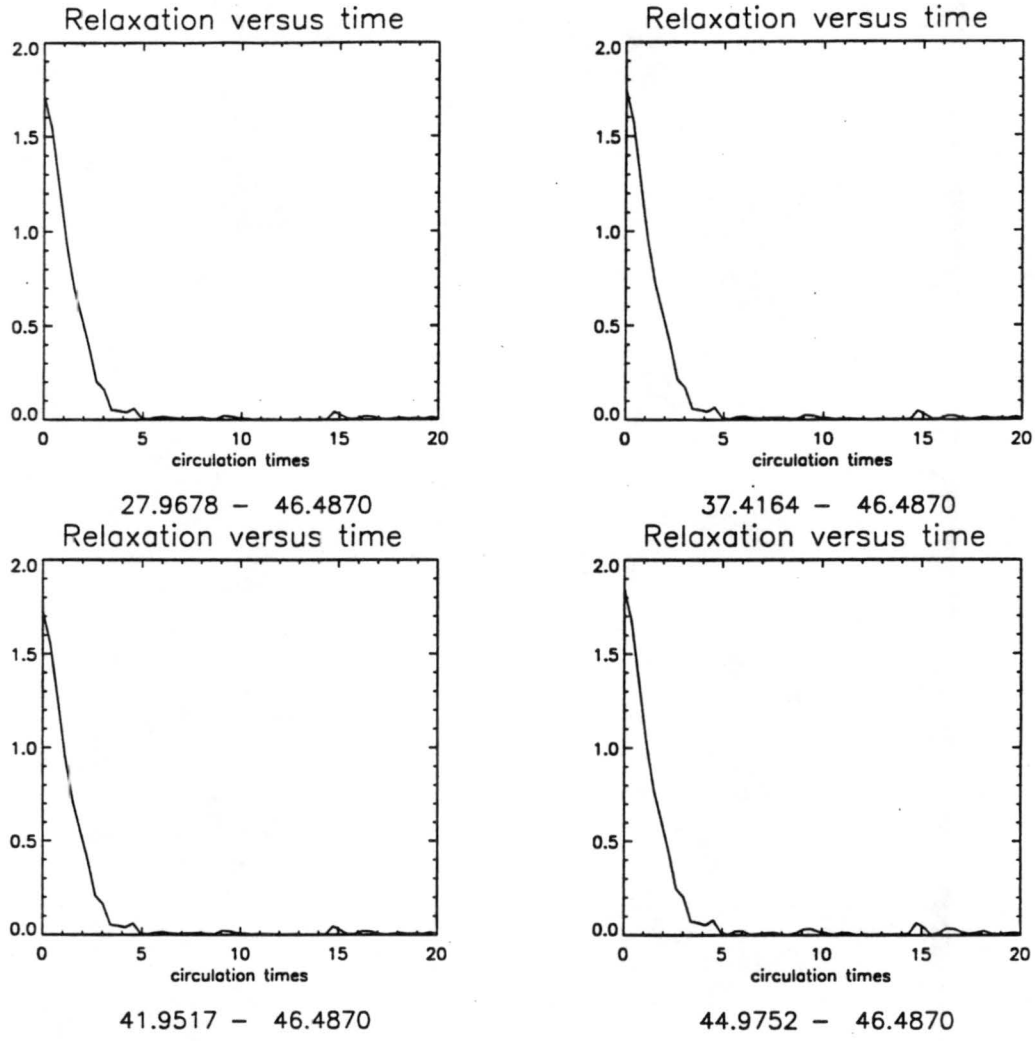

Figure 4.22: Time series of the bin-computed relaxation parameter for the `Qdense3` simulation and using four different periods for comparison.

simulation name	Relaxation time
Qdense2	6.5
Qdense3	3.5
Qdenseemily	7.5
Qdense2W	4.5
Qdense3W	3.0
b0.1Qdense2	5.0
b0.1Qdense3	2.5
b1.0Qdense2	3.0
b1.0Qdense3	2.0
b1.0Qdense2W	3.0
b1.0Qdense3W	2.0

Table 4.3: The relaxation times observed in the simulations listed. The relaxation times are reported in term of vortex mean rotational periods.

Chapter 5

CONCLUSION

The non-linear development of the interior of an unstable vortex has been investigated with a point-vortex model, and sensitivity to the initial vorticity profile has been demonstrated. It appears that the initial condition is crucial in determining the relaxed state and the speed at which the system relaxes. There is some correlation between the exponential growth rate of the initial system and the time required for relaxation, but the simulations initialized with a wider enhanced vorticity region relax more quickly than the expectation of the stability analysis. We therefore suspect that a combination of variables are important. The invariants of the initial state have to be consistent with those of the final state, but this information is insufficient to uniquely determine the relaxed state of the system. The simulations here seem to indicate that an initialization quite similar to a Rankine (top-hat) vorticity profile will find a relaxed state that is quite top-hattish, while distinctly different initializations lead to monopolar profiles.

In presenting a conceptual model for the relaxation process, we need to keep one observation in mind: the point-vortex model appears responsive to Rayleigh's sufficient criterion for stability. Where the condition is satisfied, the system maintains its character. Where an instability may be suggested by Rayleigh's necessary criterion, the system responds and changes its character. The system may be responding to the same mechanism that generates the instability suggested by a reversal in sign in the derivative in vorticity. An instability in such a system takes advantage of phasing of Rossby waves that form at the gradient in vorticity. Ordinarily these waves do not grow, but if the oppositely signed gradients in vorticity are strong enough and close enough to each other, the Rossby waves may phase lock and grow. Conceivably, the waves could grow to the point where

the disturbance is no longer of small-amplitude (as shown, for example in Appendix D). The cases presented, though, evolve without apparently such a large asymmetric response. The relaxation process may be conceptualized then as a constant process of stability testing and response, rather than the large-scale, bulk, asymmetric response suggested by Appendix D.

An alternate conceptual model is proposed here that may be consistent with the one proposed above. There is the possibility that the observed behavior may be an artifact of the point-vortex system rather than continuous-field, vorticity dynamics. In this conceptual model, the instability is realized as a local-scale influence that acts on the scale of separation of the point-vortices. Invoking the ring stability arguments of Chapter 2, a handful of nearby vortices at nearly the same radius may be conceptualized as a small segment of a ring system with the inclusion of a central vortex and an exterior vortex to approximate the circulation of the rest of the system. A strong central vortex promotes the stability of the ring segment since its only effect is to direct the vortices along their orbit without change of radius. An exterior vortex might have the opposite effect, sending vortices that are forward on the ring segment towards the center of the ring and vortices that are arears on the ring segment outward. Although this approximation would have to be considered repeatedly so that the inward and outward effects would approximately cancel for any given vortex, it suggests a source for the instability. For an unstable ring fragment (defined by a strong exterior vortex effect), a certain fraction of the vortices are directed inward and a fraction of the vortices are directed outward. The inwardly directed vortices promote the stability of the remaining vortices of the ring fragment. Since vortices are prohibited from approaching very close to each other, there is a limit to the inward propagation of vortices. Alternately, the inwardly propagating vortices may enter new ring fragments that prove to be stable. This new higher concentration of vortices at interior radii promotes the stability of more exterior radii, thus the stability of the entire vortex cloud may be established.

Of immediate interest is to extend this study to the continous domain. A Cartesian spectral model could be used to verify that the point-vortex model successfully simulates

the barotropic dynamics. If this proves successful, continued study with the point-vortex model would be desirable since the vortex can truly be studied in the most ideal conditions (frictionless flow, infinite domain) and problems can be simply reduced to a handful of parameters. The full examination of the $(\delta, v_{\tan}(\delta))$-parameter space might provide a better indication as to what influences the monopolicity of the relaxed state and time required for relaxation. The magnitude and radius of the maximum tangential wind can probably serve as a good measure of monopolicity, although this would have to be explored.

The linear stability analysis of the three-region model should be extended to the quasi-geostrophic, shallow-water system. It is further proposed that the stability analysis be carried out for more generalized representations of an unstable vortex with the two-dimensional non-divergent, quasi-geostrophic shallow-water, asymmetric balance, and primitive equation models. We might expect, from the result of Edwards (1994), to see the introduction of wavenumber 2 distrubances with the introduction of smoother vorticity profiles.

Aspects of the non-axisymmetric relaxation (illustrated in Appendix D) need to be further explored. An improved means for characterizing the two-dimensional fields in the point-vortex model may be realized by bogusing zero-circulation vortices throughout the vortex void regions to create velocity data, although limitations may exist for the technique. Since the bogussed vortices are not expressed mathematically in the invariants, there are no prohibitions that forbid the bogussed vortices from approaching to some infinitesmal distance from a point-vortex, so in practice, this technique may be unsatisfactory. The creation of a more-or-less continuous representation of the velocity field that reasonably removes the sigularities of the individual point-vortices will be required to objectively study the non-axisymmetric development of the system. If a satisfactory point-vortex method cannot be constructed, certainly insight could be found in spectral model simulations. An asymmetric balance simulation (Shapiro and Montgomery, 1993) may be ideally suited this study because of its cylindrical wavenumber representation.

Appendix A

MODEL PERFORMANCE

A.1 Integration accuracy

As an illustration, consider the 2d model, described by Equations (3.8 - 3.9). The Runge-Kutta (4th order) algorithm (Burden and Faires, 1989; Abramowitz and Stegun, 1972, p. 896) can be described as the weighted average of four forecasts. Consider the x-component forecast equation. The first forecast in the Runge-Kutte technique, X_1, is simply an Euler step

$$X_1 = X_0 + \Delta t \cdot f'\left(t = 0; (x, y) = (X_0, Y_0)\right) \tag{A.1}$$

where Δt is the time step, f' is the tendency given by the right hand side of (3.8), and (X_0, Y_0) represent the state of the system at $t = 0$. The second, third and fourth forecasts are based on tendencies found at subsequent forecast positions, but the tendencies are applied at time $t = 0$.

$$X_2 = X_0 + \Delta t \cdot f'\left(t = \frac{\Delta t}{2}; (x, y) = \left(\frac{X_1 + X_0}{2}, \frac{Y_1 + Y_0}{2}\right)\right) \tag{A.2}$$

$$X_3 = X_0 + \Delta t \cdot f'\left(t = \frac{\Delta t}{2}; (x, y) = \left(\frac{X_2 + X_0}{2}, \frac{Y_2 + Y_0}{2}\right)\right) \tag{A.3}$$

$$X_4 = X_0 + \Delta t \cdot f'\left(t = \Delta t; (x, y) = (X_3, Y_3)\right) \tag{A.4}$$

The final forecast position at time Δt is thus

$$X_{0_{\Delta t}} = \frac{1}{6}\left(X_1 + 2X_2 + 2X_3 + X_4\right). \tag{A.5}$$

The global forecast is accurate to order $O\left[(\Delta t)^4\right]$, and is therefore sensitive to selection of time step.

The time step for the simulations shown is given by

$$\Delta t = \frac{1}{25}\frac{(\Delta x)^2}{q} \tag{A.6}$$

where Δx is a typical distance seperating two close vortices, and q is the ciculation of the strongest vortex. The guiding philosphy in choosing the time step is that a vortex should not traverse a distance seperating it from another vortex in a single time step. The coefficient $\frac{1}{25}$ ensures this. A typical displacement computed with Equation (3.8) is $\frac{q}{2\pi\Delta x}\Delta t$, which is equivalent to $\frac{\Delta x}{50\pi}$.

For the `Qdense3` simulation, using Equation (A.6), the non-dimensional time step is computed, $\Delta t = 3.0 \times 10^{-2}$. The first time step of output is compared with a simulation with the same initialization, but with a time step of $\Delta t = 3.0 \times 10^{-4}$. The difference in the positions of the vortices between these two models can be considered the error of the `Qdense3` simulation. The maximum error for any vortex in the x-component of position is for vortex 247, with an error in position of $4.1659676 \times 10^{-11}$. The displacement of vortex 247 in the x-direction over the time step is 4.4395435×10^{-3}. The relative error in the x-component of position of the vortex is then 9.38377×10^{-9}. Other investigations show global similarity of the solution to a moderate amount of time with a halving of the timestep given in (A.6). At this time, non-linear interactions are leading to a divergence of the solution, but since the system is known to be chaotic, this is to be expected. The ability of the model to carry an accurate solution out to a moderate amount of time gives us confidence that the model is capturing the mean character of the solution, even if the exact, local solution cannot be captured.

The inaccuracy of the simulation can also be gauged by changes in the invariants (Equations 3.25 - 3.28). For the `Qvorts3` simulation, Table (A.1) summarizes changes in the invariants at initialization and at the end of the 25000 time step run. Since all the invariants are found to vary only minimally, we can conclude that the simulation is effective for the point-vortex model.

Verification on other simulations provide similar results.

invariant	initial value	after 25000 steps	difference
X	$9.890170060515908 \times 10^{-4}$	$9.890170060517916 \times 10^{-4}$	2.008×10^{-16}
Y	$-2.477505216096247 \times 10^{-4}$	$-2.477505216093414 \times 10^{-4}$	2.833×10^{-16}
D	.7966858368296572	.7966860877469891	2.509×10^{-7}
W	$-.100981811416007$	$-.100972816331288$	8.9951×10^{-6}

Table A.1: Initial values of the invariants X, Y, D, and W in the `Qdense3` simulation and values after 25000 times steps of fourth-order Runga-Kutta integration with a time step of 3.0×10^{-2}.

A.2 Convergence of Solution with Vortex Number and Configuration

It is assumed throughout this paper that 360 point-vortices are sufficient to properly model the relaxation processes of the vortex. Employing the initialization technique used throughout this thesis (to represent vorticity by varying the density of vortices), Figures (A.1 - A.3) show a similar character among the relaxed profiles that is independent of the number of vortices. These figures show the similarity of results with a doubling and a quadrupling of the number of vortices. The same can be seen in Figures (A.4 - A.6) employing an alternate initialization technique (to represent vorticity by varying the strength of equally spaced vortices). These results suggest that a 360 vortex model can illustrate much of the character of this simple problem.

Similarities in results can also be seen in the QGSW model. Figures (A.7) and (A.8) show many similarities to similar 2d model output (Figures A.1 and A.3) by using a small value for the inverse Rossby radius (0.1). The plots of relative vorticity have been suppressed for the small inverse Rossby radius results because they are nearly coincident with the potential vorticity profiles. Similarly, Figures (A.11) and (A.12) show a convergence in the character of their relaxed solutions and relaxation process for a larger inverse Rossby radius (1.0).

Generally, increases in the number of vortices leads to a longer period required for relaxation. But, there is evidence that the relaxation period does not grow indefinitely with number. First, we need to note that the bin relaxation parameter for the 360 vortex simulations have a much lower value in the relaxed state than model runs with fewer vortices, thus the 360 vortex simulations must obtain a more exacting standard for relaxation.

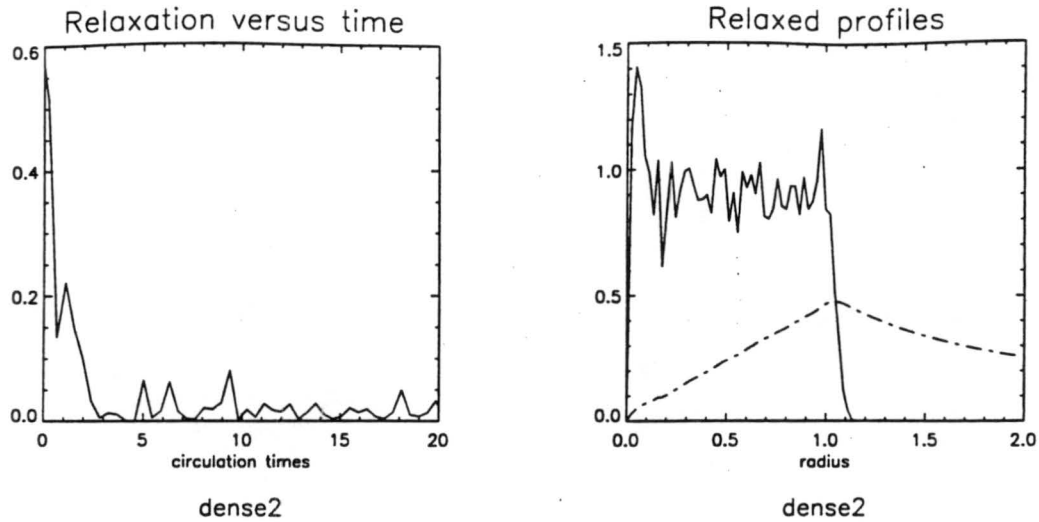

Figure A.1: (a) Time series of the bin-computed relaxation parameters for the 90 vortex **dense2** simulation and (b) profiles of the relaxed state vorticity (solid) and tangential velocity (dashed).

Additionally, we might suppose that instabilities may be enhanced in a model with few vortices, because the continuum approximation of the point-vortex model breaks down while individual vortex-vortex interactions become more important.

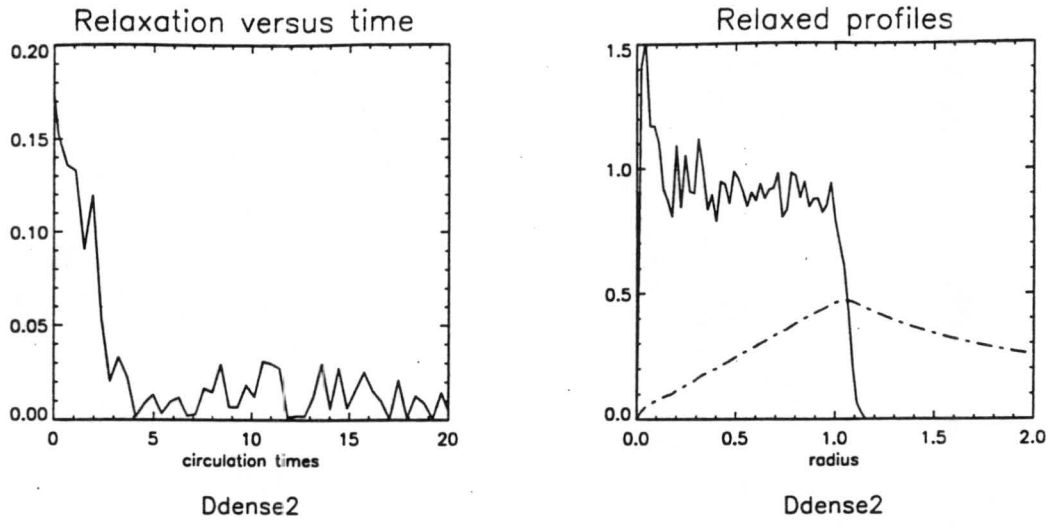

Figure A.2: (a) Time series of the bin-computed relaxation parameters for the 180 vortex **Ddense2** simulation and (b) profiles of the relaxed state vorticity (solid) and tangential velocity (dashed).

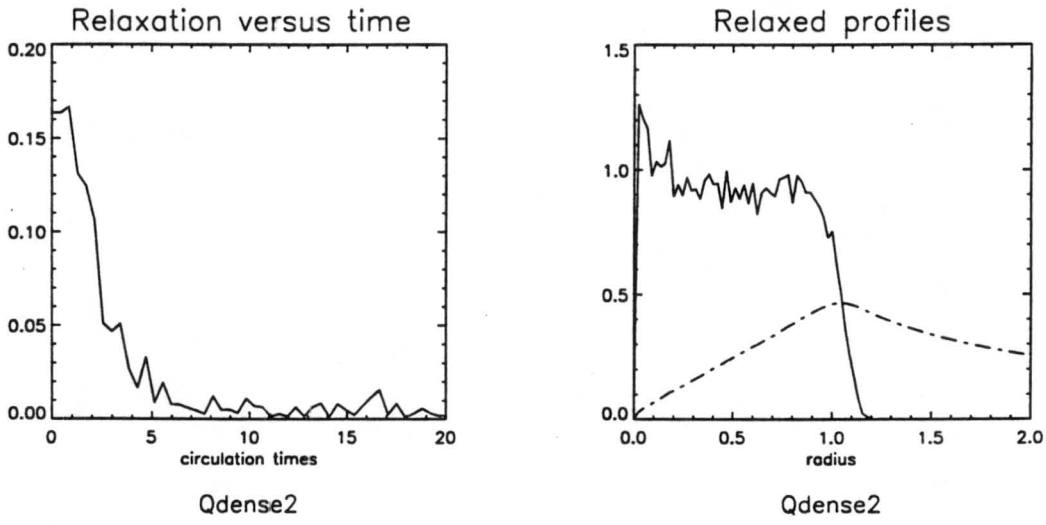

Figure A.3: (a) Time series of the bin-computed relaxation parameters for the 360 vortex **Qdense2** simulation and (b) profiles of the relaxed state vorticity (solid) and tangential velocity (dashed).

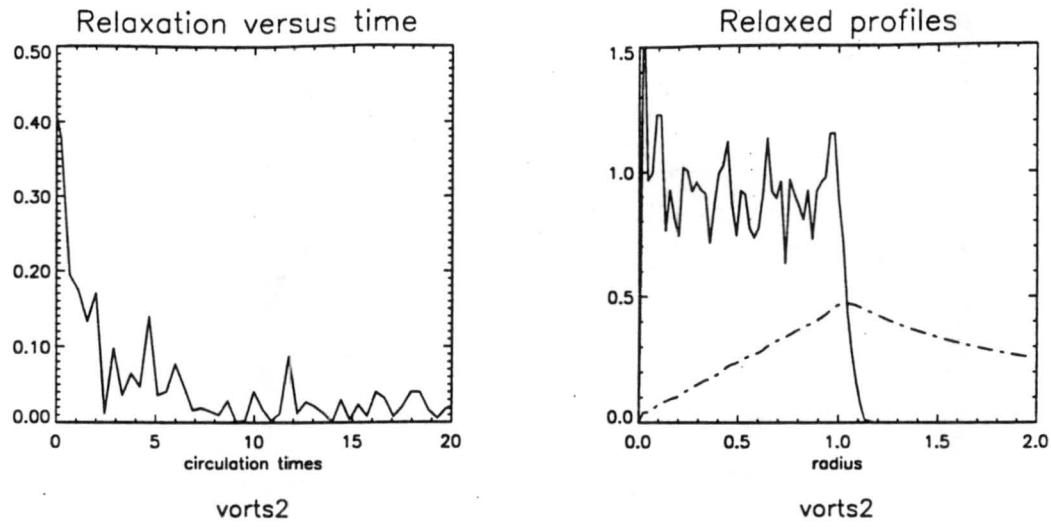

Figure A.4: (a) Time series of the bin-computed relaxation parameters for the 90 vortex `vorts2` simulation and (b) profiles of the relaxed state vorticity (solid) and tangential velocity (dashed).

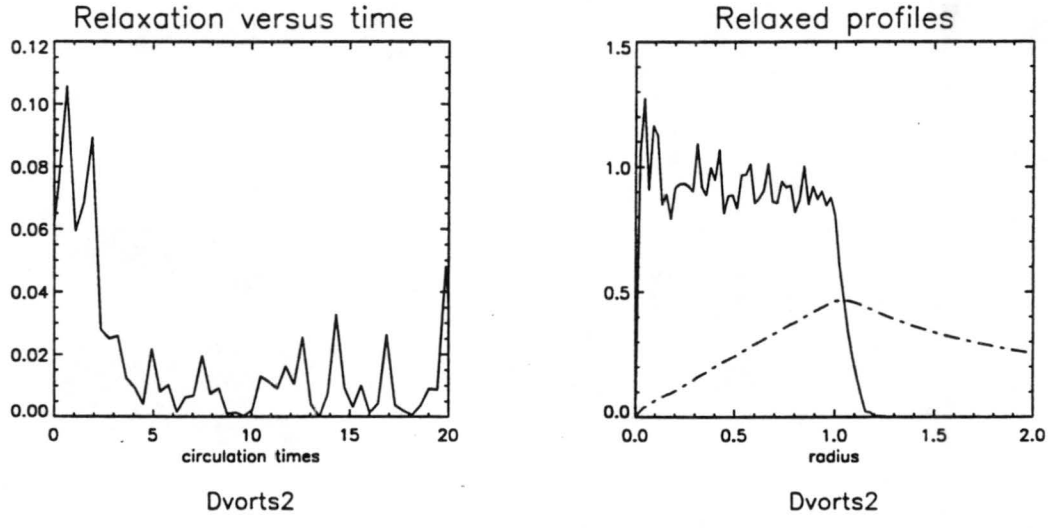

Figure A.5: (a) Time series of the bin-computed relaxation parameters for the 180 vortex `Dvorts2` simulation and (b) profiles of the relaxed state vorticity (solid) and tangential velocity (dashed).

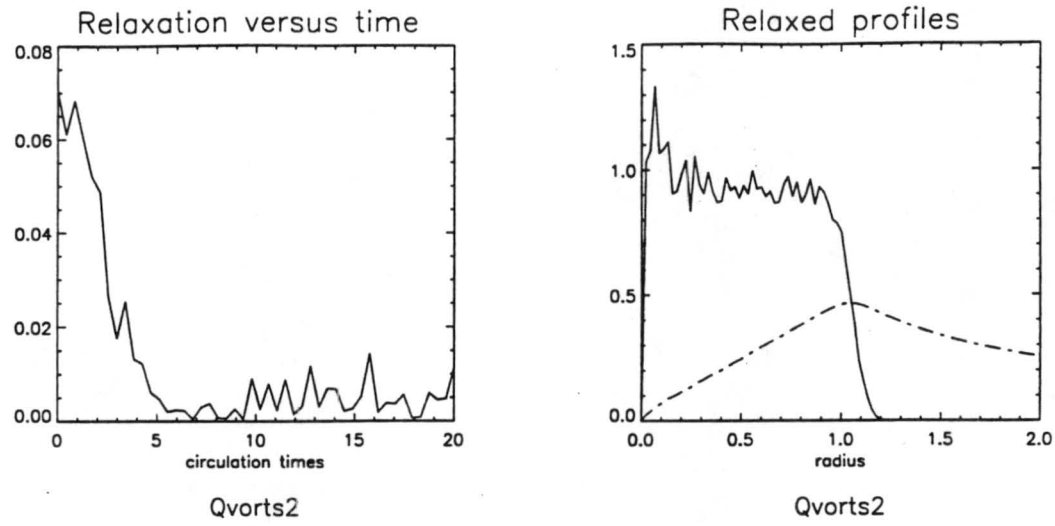

Figure A.6: (a) Time series of the bin-computed relaxation parameters for the 360 vortex `Qvorts2` simulation and (b) profiles of the relaxed state vorticity (solid) and tangential velocity (dashed).

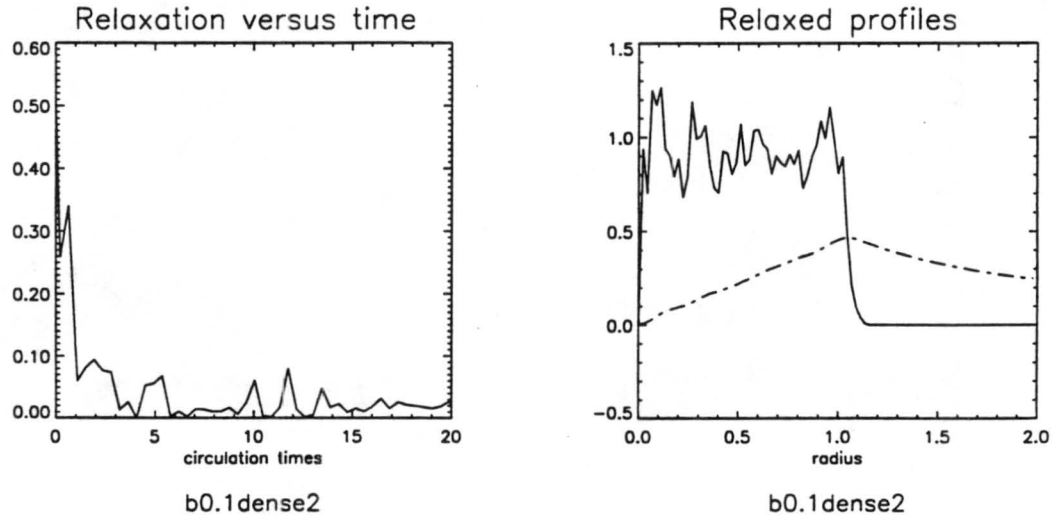

Figure A.7: (a) Time series of the bin-computed relaxation parameters for the 90 vortex `b0.1dense2` simulation and (b) profiles of the relaxed state potential vorticity (solid), vorticity (dashed), and tangential velocity (dash-dotted).

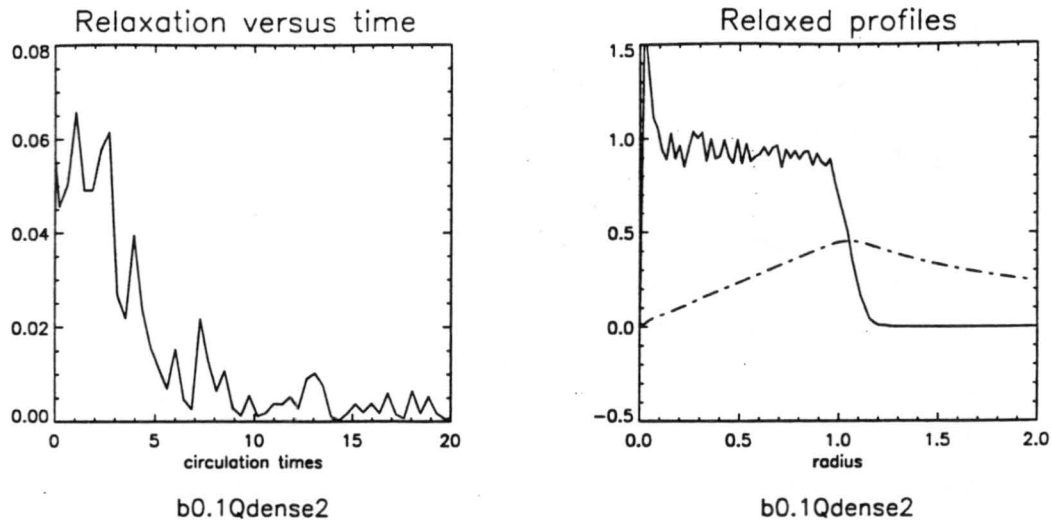

Figure A.8: (a) Time series of the bin-computed relaxation parameters for the 360 vortex `b0.1Qdense2` simulation and (b) profiles of the relaxed state potential vorticity (solid), vorticity (dashed), and tangential velocity (dash-dotted).

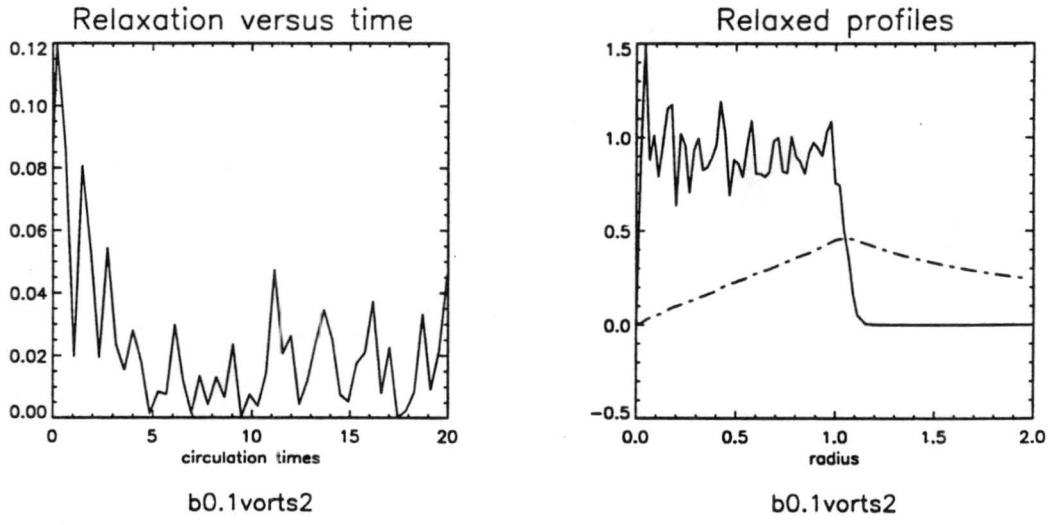

Figure A.9: (a) Time series of the bin-computed relaxation parameters for the 90 vortex `b0.1vorts2` simulation and (b) profiles of the relaxed state potential vorticity (solid), vorticity (dashed), and tangential velocity (dash-dotted).

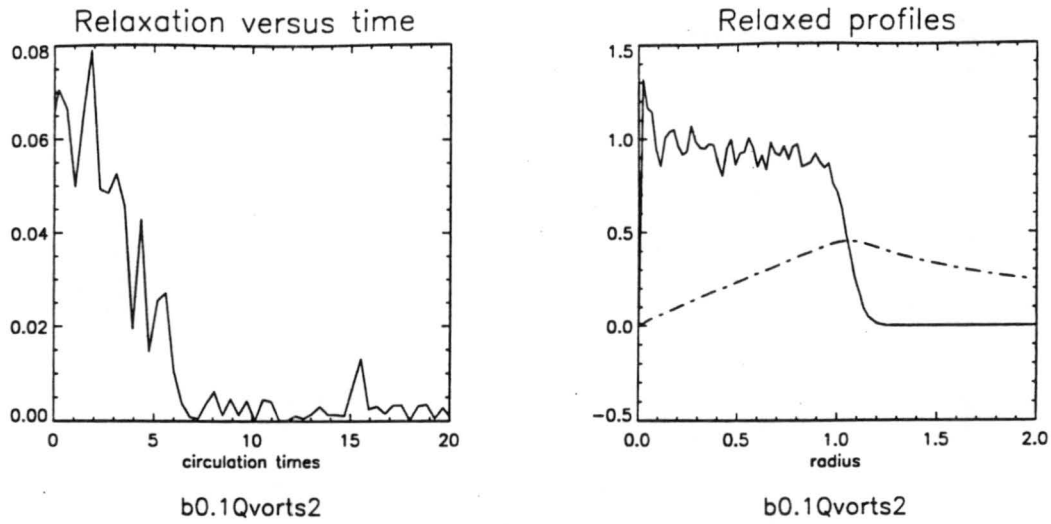

Figure A.10: (a) Time series of the bin-computed relaxation parameters for the 360 vortex `b0.1Qvorts2` simulation and (b) profiles of the relaxed state potential vorticity (solid), vorticity (dashed), and tangential velocity (dash-dotted).

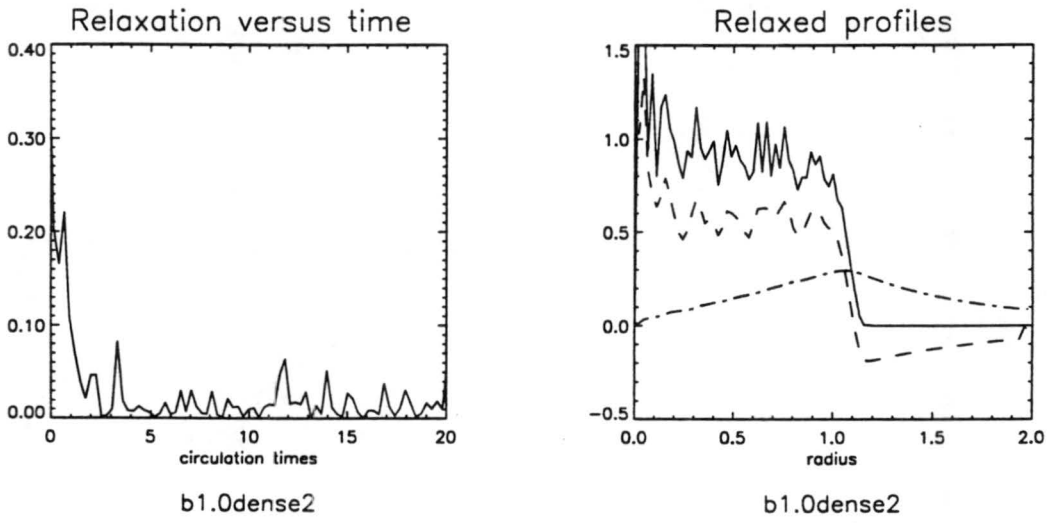

Figure A.11: (a) Time series of the bin-computed relaxation parameters for the 90 vortex `b1.0dense2` simulation and (b) profiles of the relaxed state potential vorticity (solid), vorticity (dashed), and tangential velocity (dash-dotted).

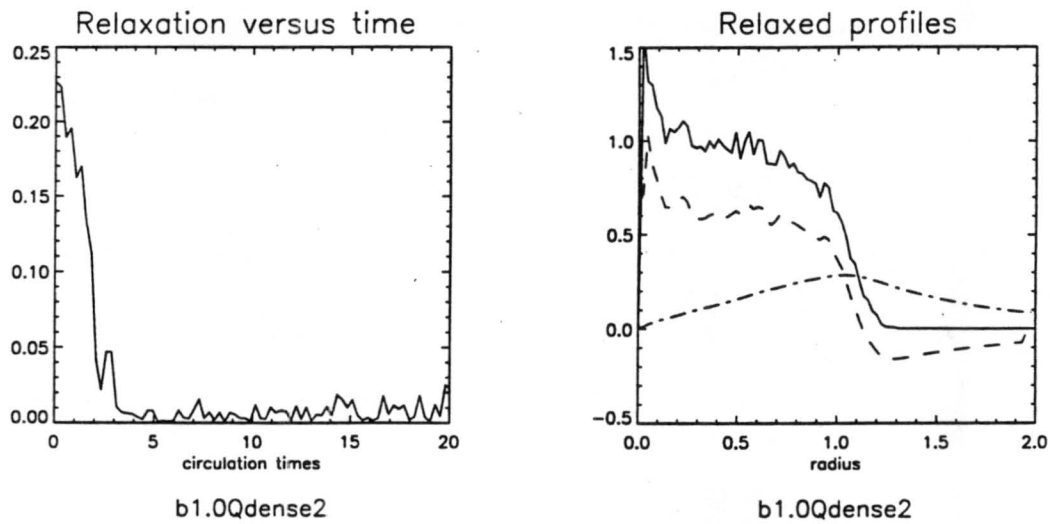

Figure A.12: (a) Time series of the bin-computed relaxation parameters for the 360 vortex `b1.0Qdense2` simulation and (b) profiles of the relaxed state potential vorticity (solid), vorticity (dashed), and tangential velocity (dash-dotted).

Appendix B

RANKINE INITIALIZATION

A logical extension of the relaxation experiments conducted for this paper is to study the behavior of a relaxed state, the Rankine vortex in particular, in the point-vortex model. Two simulations were conducted in the 2d model, one each with 360 (`Qtophat`) and 720 (`Otophat`) vortices. The distinction between **dense** initializations and `vorts` initializations is irrelevant in this case. The initial and final distributions of vortices in the `Otophat` simulation are depicted in Figure (B.1). The relaxed state for these cases (Figures B.2 and B.3), especially in the `Otophat` simulation, exhibits some different behavior than that shown in the rest of this paper.

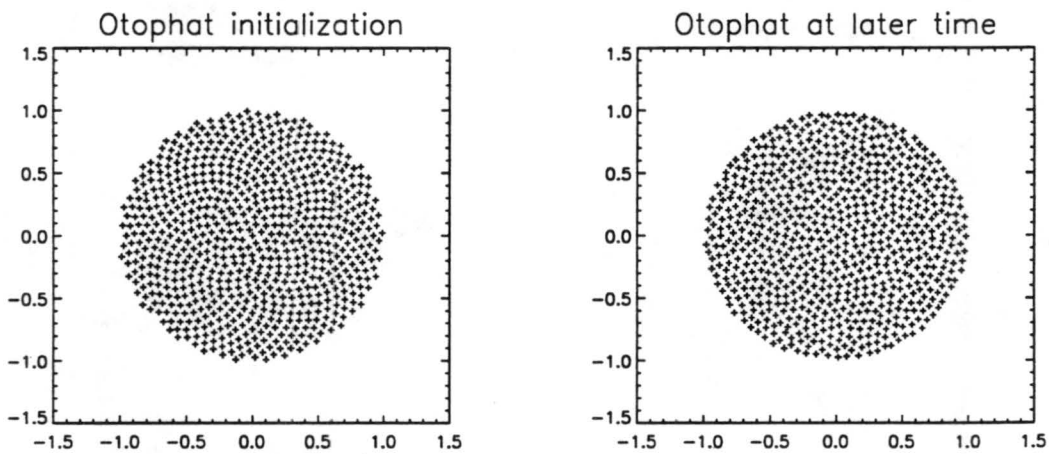

Figure B.1: The spatial distribution of vortices for the `Otophat` simulation at the (a) initial time and at (b) a much later time in the simulation.

The hypothesis of this appendix is that the behavior depicted in Figure (B.3) is a point-vortex realization of the idealized, Rankine vortex initialization. By Rayleigh's sufficient condition for stability (Gent and McWilliams, 1986), the Rankine vortex should

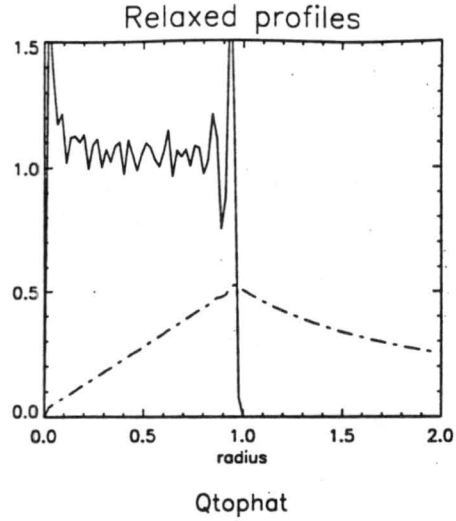

Figure B.2: (a) Time series of the bin-computed relaxation parameters for the `Qtophat` simulation and (b) profiles of the relaxed state vorticity (solid) and tangential velocity (dashed).

be stable since there is no change in sign in the derivative of vorticity (if the singularity at the radius of maximum winds is suitably handled). Similarly the radial profile of vorticity depicted in Figure (B.3) shows reversals in sign in the derivative of vorticity that satisfy the Rayleigh's necessary condition for instability, and experience from the other initializations throughout the paper would strongly suggest should be unstable. The flavor for explaining this can be had after reading Campbell and Ziff's (1979) treatment of rotating equilibrium solutions for an ensemble of vortices. As rigidly rotating equilibria, we can consider these equilibria to be approximations of a Rankine vortex. One of the results of Campbell and Ziff is that "[t]he positions of the vortices fall very closely, or exactly when symmetry allows, into concentric rings." Applying the analysis like that depicted in Figure (B.3), this equilibrium state would be realized as a sequence of spikes at discrete radii. While the radial profile depicted in Figure (B.3) does not replicate this expectation exactly, the outer and inner regions certainly capture much the flavor of such a result. Vortex streaks are shown in Figures (B.4) and (B.5) for both a short and a longer segment of the `Otophat` simulation. In the first figure, one can see that the vortex streaks have organized into certain discrete radii at many places near the outer edge of the vortex (although by no means perfectly). The same can be seen near the center of the vortex in the second figure.

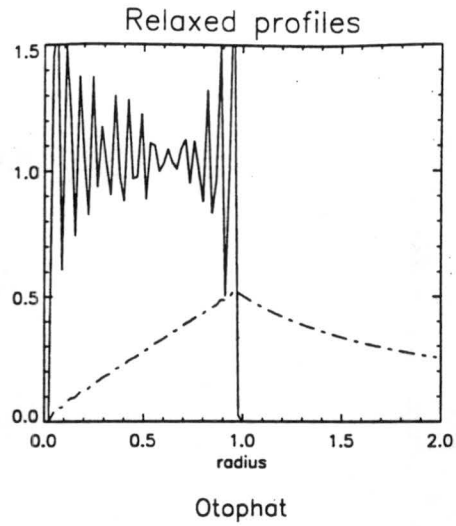

Figure B.3: (a) Time series of the bin-computed relaxation parameters for the `Otophat` simulation and (b) profiles of the relaxed state vorticity (solid) and tangential velocity (dashed).

The rest of the vortex cloud does not display behavior as coherent as the inner and outer regions.

The sharp edge in vorticity at the outer edge of the vortex, as well as the zero velocity point near the center of the vortex, seem to act locally as organizing influences upon individual point-vortices. As the vortices seem to be particularly restrained from obtaining radial positions greater than some constant (in spite of the large number of vortices very near this radius), the vortices lose some freedom of motion and thus are inclined to simply maintain this outer radius as they encounter it. Once this radius is established, some discreet radius interior should similarly be constrained, because the energy and dispersion invariants, W and D, forbid vortices from approaching arbitrarily close to each other. Similarly, the very low velocity of the center of the vortex leads to a long residency time for an individual point-vortex that should find itself in that position. The combination of invariants then would enforce some kind of likely separation at which a polygon of vortices may organize around the center of the vortex.

In the perturbed, or excited, initializations mentioned elsewhere in this paper, the local forcing due to the instability would initially override any influence for the vortex to remain constrained within some finite radius. To satisfy stability, vortices then are allowed to relax outward into a lower density region, a tail such as that exhibited in

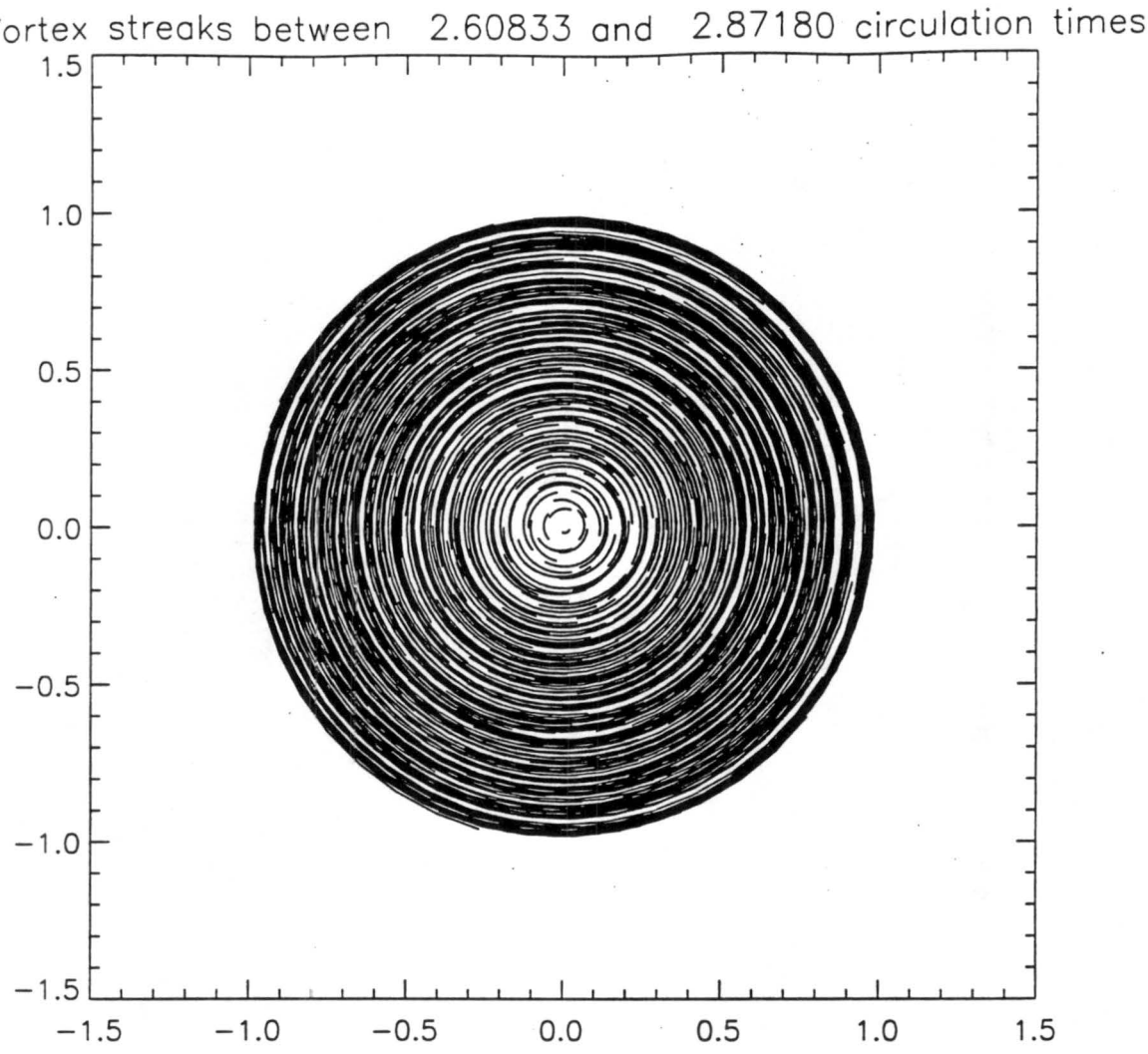

Figure B.4: Vortex streaks in the **Otophat** simulation.

Figure (4.12). This removes the organizing influence of the outer edge. Near the center, all the relaxed states of the excited initializations exhibited elsewhere in this paper show a peak in vorticity at the center of the storm. The interior of these states then are not in solid-body rotation, thus a semi-equilibrium cannot be obtained.

We are left to conclude that the behavior exhibited in the average profiles in Figures (B.2) and (B.3) are due to a peculiarity of the point-vortex representation, but do in fact represent Rankine-like, solid-body systems.

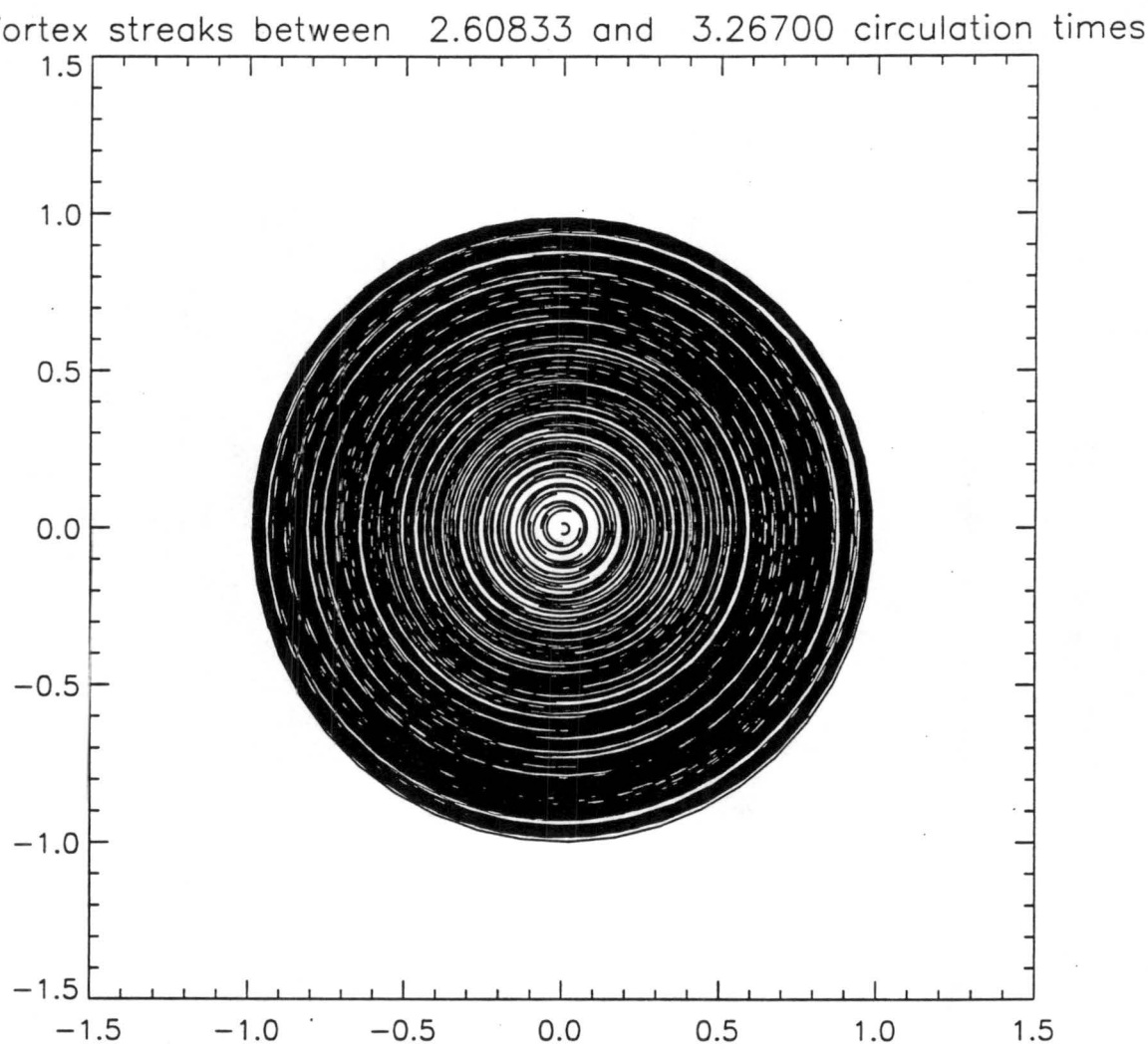

Figure B.5: Longer vortex streaks in the `Otophat` simulation.

Appendix C

PROCEDURE FOR INITIALIZATION

The locations of the point-vortices at initialization are positioned so as to most reasonably mimic the desired axisymmetric profile of vorticity. Each point-vortex is assigned a unique radial position. The angular positions of the point-vortices are determined with a weight minimization procedure so that they are evenly distributed.

Radial Positions

dense *initializations*

In order to determine the radial positions of the point-vortices for the **dense** family of simulations, consider an initially, axisymmetric vorticity distribution, $\bar{\zeta}(r)$ (the concepts extend to the QGSW model with the appropriate substitution of potential vorticity for vorticity). The total circulation contained within the entire domain is

$$\Gamma = \int_0^\infty 2\pi r \bar{\zeta}(r) \mathrm{d}r \tag{C.1}$$

which is typically set to π for the purposes of the non-dimensionalization presented in this thesis. In the cases considered here, $\bar{\zeta}$ is a positive function, therefore, a monotonic increasing function can be defined

$$g(r) = \int_0^r 2\pi r \bar{\zeta}(r) \mathrm{d}r. \tag{C.2}$$

Since $\bar{\zeta}$ is circularly symmetric, g represents the circulation of a circle of radius r. If we were to discretize the circulation into N equal levels, a radial position would be defined by (C.2) at every location where g increases by a discrete amount. Define the radial position of the n-th vortex as

$$g(r_n) = \Gamma \cdot \frac{n}{N}. \tag{C.3}$$

Consider the simplest case where $\bar{\zeta}(r) = 1$ inside a circle of radius unity.

$$\Gamma = \int_0^1 2\pi r \mathrm{d}r = \pi \tag{C.4}$$

and

$$g(r) = \int_0^r 2\pi r \mathrm{d}r = \pi r^2 \tag{C.5}$$

so solving for r_n in (C.3) gives

$$r_n = \sqrt{\frac{n}{N}}. \tag{C.6}$$

Arbitrary functions for $\bar{\zeta}$ may be considered in the same way as long as $\bar{\zeta}$ is strictly positive.

`vorts` *initializations*

The method of determining the unique radial positions of the point-vortices for the `vorts` family of simulations is simply (C.6) (as if $\bar{\zeta} = 1$, assuring equal distribution). The strength of the n-th vortex is assigned for an arbitrary function $\bar{\zeta}$ defined on $0 \leq r \leq 1$ by

$$q_n = 2\pi r \cdot \delta r_n \cdot \bar{\zeta}\left(\sqrt{\frac{n}{N}}\right) \tag{C.7}$$

where δr_n may be defined from direct computation of the radial positions of the neighboring points

$$\delta r_n = \frac{r_{n+1} - r_{n-1}}{2}. \tag{C.8}$$

Angular Positions

The angular positions are determined by a weight minimization procedure in order to avoid clumping. An iterative procedure is described below, but in practice only the zeroth iteration is necessary to produce satisfactory results for the majority of initializations considered in this work. The elliptical vortex simulation of Figure (1.4) was the only exception where an iterative procedure was found to be neccessary. The zeroth iteration locates a given vortex based only on information interior to it, since the outer vortices have not been located yet. Further iterations locate the vortex based on information from all the vortices.

The procedure first assumes that the radial positions of the vortices are known. To determine the angular position of the current vortex, define an array to discretize the

circle that lies at the radius of this vortex. For example, for the cases considered in this work, the vortex is located at one of 300 equally spaced angular positions. At each point in the array, the induced wind speed is individually computed from each point-vortex and is summed as a measure of nearness to other point vortices. The vortex then is located where this function is minimized.

Appendix D

A CASE OF STRONGLY NON-AXISYMMETRIC RELAXATION

The main body of this thesis describes the relaxation of the three-region vortex cloud that displays a nearly axisymmetric response. This appendix describes a three-region vortex cloud displaying a highly non-axisymmetric response.

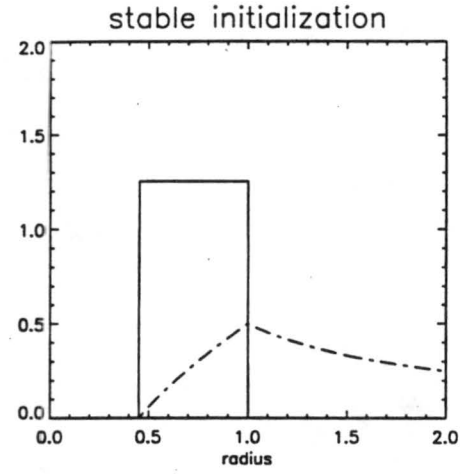

Figure D.1: Profiles of the initial state vorticity (solid) and tangential velocity (dashed) for the **densestable** simulation.

The initial profiles in vorticity and wind are displayed in Figure (D.1). The Michalke and Timme (1967) analysis for this case shows stability ($\delta = 0.45$, $v_{\tan}(\delta) = 0.0$) (Figure 2.3).

Figure (D.2) shows vortex streaks for four time intervals that depict the transition from where a wavenumber four disturbance is evident in the interior of the vortex to where wavenumber three dominates. Figure (D.3) continues this sequence from the beginnings of a noticeable wavenumber two disturbance to the development of a wavenumber one disturbance. All eight figures are separated by an equal interval of time. Of note is the

figure beginning at 6.6 circuit periods, where the central region void of vorticity begins to be ejected from the center. A similar process is described by Ishioka and Yoden (1994) in a spectral model, but they attribute the effect to the spherical curvature of their domain.

Although this development is distinctly non-axisymmetric, the axisymmetric analyses of Chapter 4 are depicted in Figure (D.4). Of note is that since the circulation has been deposited in a much wider range of radii, the vorticity throughout the vortex is weaker. Figure (D.5) depicts the locations of vortices at initialization and at a much later time when apparent asymmetries have settled down.

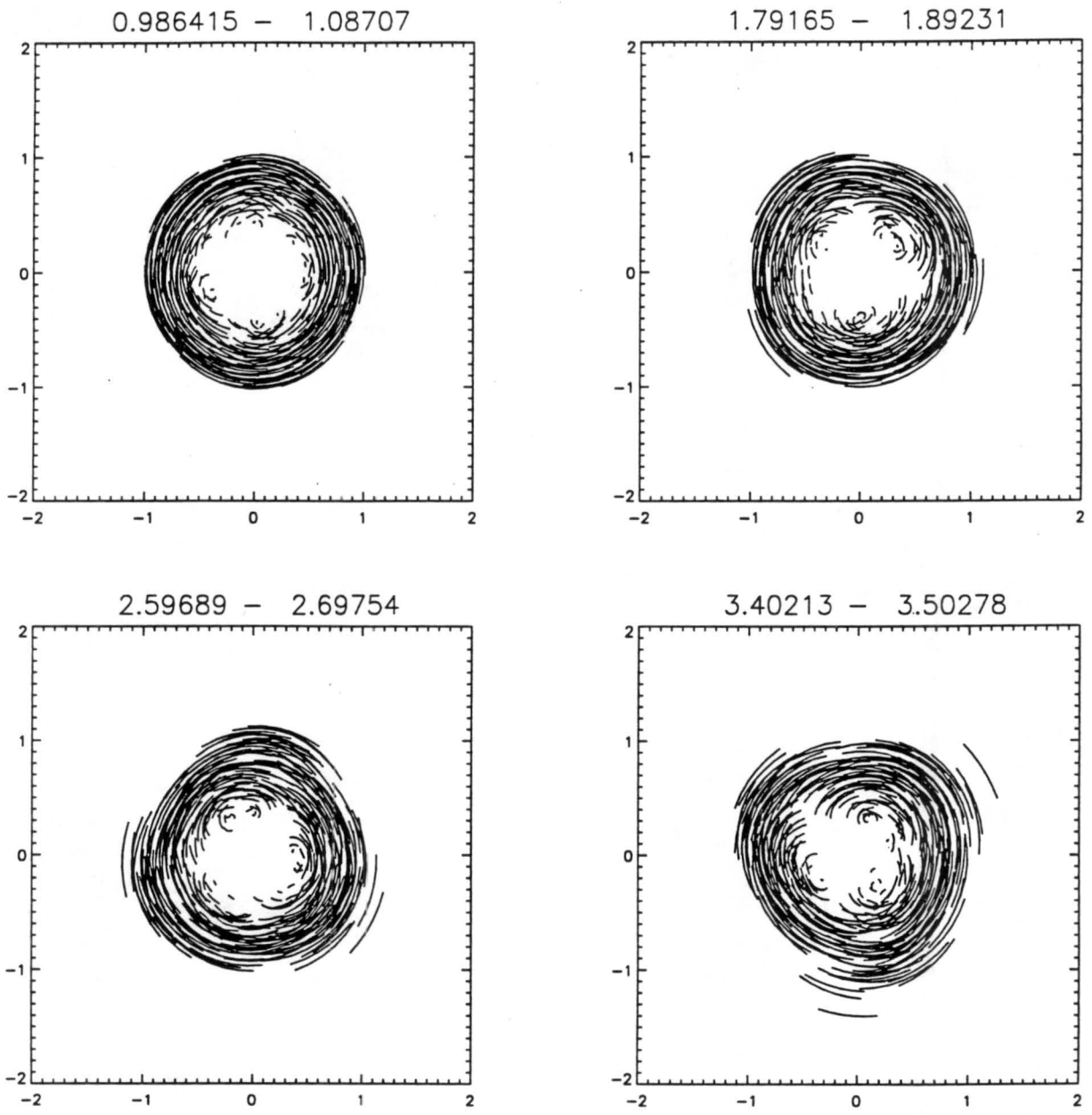

Figure D.2: Vortex streaks for the `Qdensestable` simulation for the circuit time intervals listed above each figure.

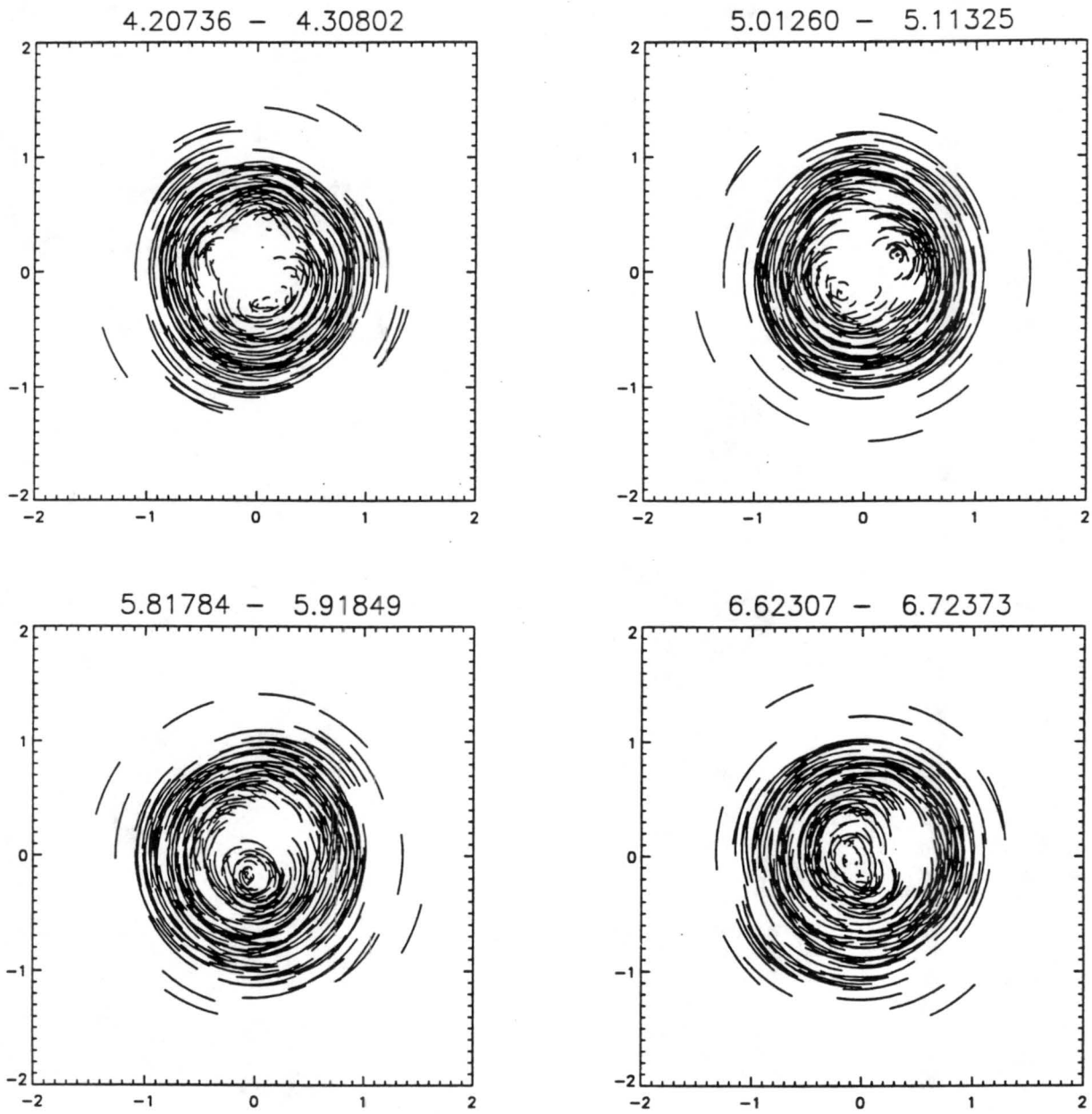

Figure D.3: Vortex streaks for the `Qdensestable` simulation for the circuit time intervals listed above each figure.

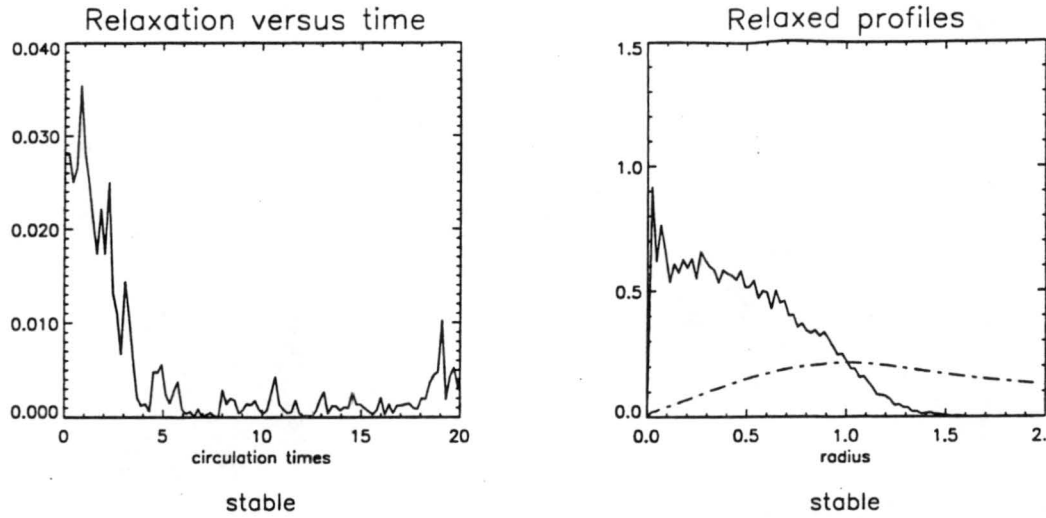

Figure D.4: (a) Time series of the bin-computed relaxation parameters for the `Qdensestable` simulation and (b) profiles of the relaxed state vorticity (solid) and tangential velocity (dashed).

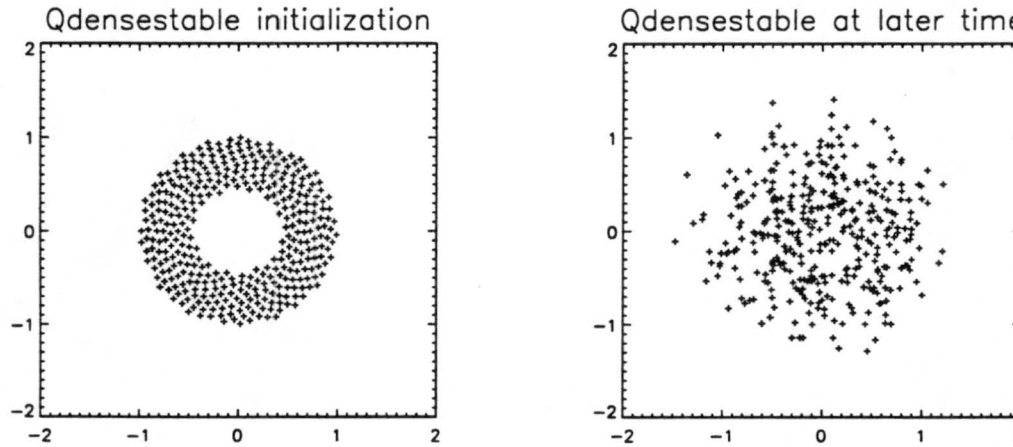

Figure D.5: Snaphots of the locations of the point vortices in the `Qdensestable` simulation at (a) initialization and at (b) a much later time.

REFERENCES

Abramowitz, M., and Stegun I.A., 1972: Handbook of mathematical functions. Dover Publications, New York: ninth printing.

Aref, H., 1983: Integrable, chaotic, and turbulent vortex motion in two-dimensional flows. *Ann. Rev. Fluid Mech.*, **15**, 345–389.

Batchelor, G.K., 1967: An introduction to fluid dynamics. Cambridge University Press, Cambridge.

Burden, R.L., and J.D. Faires, 1989: Numerical Analysis. Fourth Edition. PWS-Kent Publishing, Boston.

Burpee, R.W., S.D. Aberson, P.G. Black, M. DeMaria, J.L. Franklin, J.S. Griffin, S.H. Houston, J. Kaplan, S.J. Lord, F.D. Marks Jr., M.D. Powell, and H.E. Willoughby, 1994: Real-time guidance provided by NOAA's hurricane research division to forecasters during Emily of 1993. *Bull. Am. Met. Soc.*, **75**, 1765–1783.

Campbell, L.J., and R.M. Ziff, 1979: Vortex patterns and energies in a rotating superfluid. *Phys. Rev. B*, **20**, 1886–1902.

Carnevale, G.F., J.C. McWilliams, Y. Pomeau, J.B. Weiss, and W.R. Young, 1991: Evolution of vortex statistics in two-dimensional turbulence. *Phys. Rev. Letters*, **66**, 2735–2737.

Edwards, J., 1994: Barotropic instability in the inner core of tropical cyclones. *Colorado State University*, Atmospheric Science Paper No. 552.

Fornberg, B., 1977: A numerical study of 2-D turbulence. *J. Compu. Phys.*, **25**, 1–31.

Gent, P.R., and J.C. McWilliams, 1986: The instability of barotropic circular vortices. *Geophys. Astrophys. Fluid Dynamics*, **35**, 209–233.

Guinn, T.A., and W.H. Schubert, 1993: Polygonal Eyewalls in Hurricanes. *20st Conference on Hurricanes and Tropical Meteorology*, American Meteorological Society, Boston.

Havelock, T.H., 1941: The stability of motion of rectilinear vortices in ring formation. *Phil. Mag.*, **11**, 617–633.

Ishioka, K., and S. Yoden, 1994: Non-linear evolution of a barotropically unstable circumpolar vortex. *J. Met. Soc. Japan*, **72**, 63–80.

Kasahara, A., 1957: The numerical prediction of hurricane movement with the barotropic model. *J. Meteor.* , **14**, 386–402.

———, and G.W. Platzman, 1963: Interaction of a hurricane with the steering flow and its effect upon the hurricane trajectory. *Tellus*, **15** , 321–335.

Lilly, D.K., 1969: Numerical simulation of two-dimensional turbulence. *Phys. Fluids Suppl. II: High Speed Computing in Fluid Dynamics*, 240–249.

Melander, M.V., J.C. McWilliams, and N.J. Zabusky, 1987: Axisymmetrization and vorticity-gradient intensification of an isolated two-dimensional vortex through filamentation. *J. Fluid Mech.*, **178**, 137–159.

———, N.J. Zabusky, and J.C. McWilliams, 1988: Symmetric vortex merger in two dimensions: causes and conditions. *J. Fluid Mech.*, **195**, 303–340.

Möller, J.D., and R.K. Smith, 1994: The development of potential vorticity in a hurricane-like vortex. *Q.J.R. Meteorol. Soc.*, **120**, 1255–1265.

Morikawa, G.K., 1962: On the prediction of hurricane tracks using a geostrophic point vortex. *Proceedings of the International Symposium on Numerical Weather Prediction in Tokyo* , Meteorological Society of Japan, Tokyo. 349–360.

———, and E.V. Swenson, 1971: Interacting motion of rectilinear geostrophic vortices. *Phys. Fluids*, **14**, 1058–1073.

McWilliams, J.C., 1985: The emergence of isolated coherent vortices in turbulent flow. *J. Fluid Mech.*, **146**, 21–43.

Novikov, E.A., 1976: Dynamics and statistics of a system of vortices. *Sov. Phys.-JETP*, **41**, 937–943.

Onsager, L., 1949: Statistical hydrodynamics. *Nuovo Cimento*, **6** (Suppl. No. 2), 279–287.

Shapiro, L.J., and M.T. Montgomery, 1993: A three-dimensional balance theory for rapidly rotating vortices. *J. Atmos. Sci.*, **50**, 3323–3335.

Stewart, H.J., 1943: Periodic properties of the semi-permanent atmospheric pressure systems. *Q. Appl. Math.*, **51**, 262–267.

Thomson, J.J., 1883: A treatise on the motion of vortex rings. Reprinted by Dawsons of Pall Mall, London, 1968.

Viecelli, J.A., 1994: Persistence of Lagrangian trajectories in rotating two-dimensional turbulence. *J. Atmos. Sci.*, **51**, 337–352.

Weiss, J.B., and J.C. McWilliams, 1991: Nonergodicity of point vortices. *Phys. Fluids A*, **3**, 835–844.

Whitaker, N., and B. Turkington, 1994: Maximum entropy states for rotating vortex patches. *Phys. Fluids*, **6**, 3963–3973.

Zabusky, N.J., M.H. Hughes, and K.V. Roberts, 1979: Contour-dynamics for the Euler equations in two dimensions. *J. Comput. Phys.*, **30**, 96–106.